

AD-A234 647

2

REPORT NO.

AERO-OPTICS ANALYSIS

DR. L. D. RUSSELL

CLEARED  
FOR OPEN PUBLICATION 25 MAR 1991  
U.S. ARMY STRATEGIC DEFENSE COMMAND  
PUBLIC AFFAIRS OFFICE  
THE UNIVERSITY OF ALABAMA HUNTSVILLE  
School of Engineering  
Huntsville, AL 35899

JANUARY 1991

DTIC  
ELECTED  
APR 09 1991  
S C D

ANNUAL REPORT  
28 September 1989 - 30 September 1990  
DASG60-89-C-0145

SPONSORED BY  
U. S. ARMY STRATEGIC DEFENSE COMMAND

PREPARED FOR:  
U.S. Army Strategic Defense Command  
P.O. Box 1500  
Huntsville, AL 35807-3801

ADMINISTERED BY:  
OFFICE OF NAVAL RESEARCH  
Atlanta Area Office  
Georgia Institute of Technology  
206 O'Keefe  
Atlanta, GA 30332

The views, opinions, and/or findings contained in this report are those of the author(s) and should not be construed as an official Department of the Army position, policy, or decision, unless so designated by other official documentation.

DTIC FILE COPY

91 4 08 035



The University  
Of Alabama  
In Huntsville

Huntsville, Alabama 35899

AERO-OPTICS ANALYSIS

CONTRACT DASG60-89-C-0145

ANNUAL REPORT

for period

28 September 1989 - 30 September 1990

Accession No.	
DASG60-89-C-0145	
Type of Report	
Annual Progress Report	
Date of Report	
28 September 1990	
Distribution	
Approved by Director	
Approved by Manager	
Dist	Superal
A-1	

Principal Investigator: Dr. Lynn D. Russell  
Dean of Engineering

Contributors: Dr. M. Abushagur  
Dr. R. Adhami  
Dr. C. P. Chen  
Dr. S. Graves  
Dr. J. Jarem  
Dr. C. Katsinis  
Dr. A. Poularikas  
Dr. A. Ritter  
Dr. J. E. Smith, Jr.  
Dr. J. Ziebarth



## REPORT DOCUMENTATION PAGE

Form Approved:  
OMB No. 0704-0188

1a. REPORT SECURITY CLASSIFICATION <b>UNCLASSIFIED</b>		1b. RESTRICTIVE MARKINGS	
2a. SECURITY CLASSIFICATION AUTHORITY		3. DISTRIBUTION / AVAILABILITY OF REPORT	
2b. DECLASSIFICATION / DOWNGRADING SCHEDULE			
4. PERFORMING ORGANIZATION REPORT NUMBER(S)  UAH01/A006		5. MONITORING ORGANIZATION REPORT NUMBER(S)	
6a. NAME OF PERFORMING ORGANIZATION  Univ. of Al. in Huntsville	6b. OFFICE SYMBOL <i>(if applicable)</i> UAH/CE	7a. NAME OF MONITORING ORGANIZATION	
6c. ADDRESS <i>(City, State, and Zip Code)</i>  University of Alabama in Huntsville Huntsville, AL 35899		7b. ADDRESS <i>(City, State, and Zip Code)</i>  U.S. Army Strategic Defense Command P.O. Box 1500 ATTN: CSSD-H-QE Huntsville, AL 35807-3801	
8a. NAME OF FUNDING / SPONSORING ORGANIZATION	8b. OFFICE SYMBOL <i>(if applicable)</i>	9. PROCUREMENT INSTRUMENT IDENTIFICATION NUMBER  DASG60-89-C-0145	
8c. ADDRESS <i>(City, State, and Zip Code)</i>		10. SOURCE OF FUNDING NUMBERS  PROGRAM ELEMENT NO.      PROJECT NO.      TASK NO.      WORK UNIT ACCESSION NO.	
11. TITLE <i>(INCLUDE SECURITY CLASSIFICATION)</i> Annual Report (unclassified)			
12. PERSONAL AUTHOR(S) Russell, Lynn Dr.			
13a. TYPE OF REPORT Annual Technical	13b. TIME COVERED FROM 89-9-28 TO 90-9-30	14. DATE OF REPORT <i>(Year, Month, Day)</i> 90-12-18	15. PAGE COUNT 80
16. SUPPLEMENT NOTATION			
17. COSATI CODES  FIELD    GROUP    SUB-GROUP	18. SUBJECT TERMS <i>(Continue on reverse if necessary and identify by block number)</i>  interceptor missiles, image analysis, electromagnetic windows, supersonic/hypersonic CFD codes, window cooling, aero-optics,		
19. ABSTRACT <i>(Continue on reverse if necessary and identify by block number)</i>  The U.S. Army Strategic Defense Command (USASDC) has several ongoing and planned programs that utilize optical sensors aboard missiles traveling at hypersonic velocities in the atmosphere. Central to the missile homing problem are aero-optical effects upon a missile-born sensor/seeker which looks through both an electromagnetic window and the flow field about the vehicle. Aspects of the problem include modeling and simulation of the flow field on incident radiation from a target, and finally, predicting the resultant image imperfections and error in apparent object position as perceived by the sensor.			
20. DISTRIBUTION / AVAILABILITY OF ABSTRACT  <input type="checkbox"/> UNCLASSIFIED/UNLIMITED <input type="checkbox"/> SAME AS RPT. <input type="checkbox"/> DTIC USERS		21. ABSTRACT SECURITY CLASSIFICATION	
22a. NAME OF RESPONSIBLE INDIVIDUAL		22b. TELEPHONE <i>(Include Area Code)</i>	22c. OFFICE SYMBOL

12. Abushagur, M. Dr.  
Adhami, R. Dr.  
Chen, C. P. Dr.  
Graves, S. Dr.  
Jarem, J. Dr.  
Katsinis, C. Dr.  
Pouliarikas, A. Dr.  
Ritter, A. Dr.  
Smith, J.E. Dr.  
Ziebarth, J. Dr.
18. hypersonic shear layers, hypersonic testing, non-intrusive instrumentation, aerodynamic heating
19. The University of Alabama in Huntsville is engaged in a program of aero-optics research and development in which the broad objectives are to: develop and maintain an aero-optics data base; investigate key issues in the areas of aero-optic effects; and increase synergism among ongoing efforts in aero-optics both nationally and internationally if applicable.

The aero-optics data base is a computerized data management system to house aerodynamic data related to optics, optics data related aerodynamics, and aero-optics interrelated data that is applicable to USASDC projects and missions. UAH is collecting and updating pertinent, existing data from test and analysis and will update the data base with appropriate new data from as these data are obtained. UAH is developing a data acquisition format for laboratory tests, wind tunnel tests, sled tests and flight tests to meet the needs of potential users, e.g., sensor designers and/or sensor requirements generators. Moreover, UAH is also developing criteria for the admission of data to the data base.

Data base development is supported from three other phases of the program, namely, analytical investigations, assessment of measurement techniques, and experiments on hypersonic shear flow simulation. As part of the analytical effort, UAH is surveying, reviewing, collecting, updating and using available aero-optical mathematical models and computer simulations. In assessing measurement techniques, UAH is concentrating on non-intrusive schemes such as holography, optical tomography, laser induced fluorescence and improved standard flow visualization such as Schlieren and shadowgraph. Finally, in the experimental support, UAH is setting up laboratory experiments. The flow lab experiments will utilize a flow channel having low supersonic capability. This will be used for studies and assessment of non-intrusive measurement techniques.

This annual report summarizes progress during the past year.

## AERO-OPTICS ANALYSIS

Contract DASG60-89-C-0145

### INTRODUCTION

The U.S. Army Strategic Defense Command (USASDC) has several ongoing and planned programs that utilize optical sensors aboard missiles traveling at hypersonic velocities in the atmosphere. Central to the missile homing problem are aero-optical effects upon a missile-borne sensor/seeker which looks through both an electromagnetic window and the flow field about the vehicle. Aspects of the problem include modeling and simulation of the flow field, modeling and simulation of the effects of the flow field on incident radiation from a target, and finally, predicting the resultant image imperfections and error in apparent object position as perceived by the sensor.

The University of Alabama in Huntsville is engaged in a program of aero-optics research and development in which the broad objectives are to: develop and maintain an aero-optics data base; investigate key issues in the areas of aero-optic effects; and increase synergism among ongoing efforts in aero-optics both nationally and internationally if applicable.

The aero-optics data base is a computerized data management system to house aerodynamic data related to optics, optics data related to aerodynamics, and aero-optics interrelated data that is applicable to USASDC projects and missions. Data shall be from both test and analysis. UAH will collect and update pertinent, existing data and will update the data base with appropriate new data as these data are obtained/generated. Further, UAH will develop a data acquisition format for laboratory tests, wind tunnel tests, sled tests and flight tests to meet the needs of potential users, e.g., sensor designers and/or sensor requirements generators. Moreover, UAH will also develop criteria for the admission of data to the data base.

Support for data base development will come from three other phases of the program, namely, analytical investigations, assessment of measurement techniques, and experiments on hypersonic shear flow simulations. As part of the analytical effort, UAH is surveying, reviewing, collecting, updating and using available aero-optical mathematical models and computer simulations. In assessing measurement techniques, UAH is concentrating its effort on non-intrusive schemes such as holography, optical tomography, laser induced fluorescence and improved standard flow visualization such as Schlieren and shadowgraph. Finally in the experimental support, UAH is setting up a laboratory experiment which will utilize a flow channel having low supersonic capability. This will be used for studies and assessment of non-intrusive measurement techniques.

The following sections of this report have been prepared by individual investigators and convey progress on various facets of the overall program. Each section is self-contained and can be read as an entity in itself. Specifically, these are presented as follows:

- Aero-Optics Analytical Studies - Dr. C. P. Chen
- Non-Intrusive Measurement Techniques - Dr. J. E. Smith, Jr.
- UAH Aero-Optics Data Base - Dr. J. Ziebarth  
Dr. S. Graves
- Optical Measurement Techniques - Dr. M. Abushagur
- Image Restoration by Least Squares (Wiener) Filter -  
Mr. K. S. Kim
- Mutual Coherence Propagation in Turbulent Media -  
Mr. A. Monteiro  
Dr. J. Jarem

## Aero-Optics Analytical Studies

by

C. P. Chen

### Objective

The objective of the analytical studies is to survey and evaluate current computational fluid dynamics codes for predicting turbulent shear layers above optical windows. Current state-of-the-art physical modeling, in terms of turbulence and real gas effects, is also reviewed and assessed.

### Technical Problems

The turbulent mixing shear layers over optical windows (created by a slot wall cooling jet) of hypersonic vehicles cause severe limitations to target detection and recognition. Further, if the wall jet nozzle is not properly expanded, a series of oblique shocks and expansion wave can also form above the window. Thus, in a coupled aerodynamic-optical analysis, the fluid dynamics analysis must predict not just pressure and velocities, but also steady and unsteady density fields. In aero-optics applications, variable density effects are primarily caused by the mixture of gases with different densities, strong temperature gradients within the fluid, strong distortion of shock-boundary layer interactions and compressibility effects in high speed flows. The Mach number and Reynolds number of a typical operating flight envelope precluded the use of most traditional aero-dynamic design methodologies. In such approaches, simplified analyses are combined with experimentally generated engineering correlations. To supplement or replace these traditional design methods, computational fluid dynamics (CFD) techniques are being utilized as a design tool over portions of the flight envelope where experimental data cannot be obtained economically or feasibly. Despite the current maturity of state-of-the-art CFD codes, much work remains to be done before they can be used with confidence in a design or diagnostic environment.

### General Methodology

The first step in applying CFD methods to Aero-optics flow applications was to conduct a survey to identify CFD codes in the public domain, i.e., available from government, industries and university sources. Due to strong shear and turbulence effects in the flow fields related to aero-optics, Euler codes such as CM3D and Eagle were not included. The capabilities of the applicable viscous codes identified in this survey are summarized in Table 1. In selecting these codes, special attention was paid to the code's capabilities in handling turbulence and real gas, chemical reacting flows. Both Parabolized Navier-Stokes (PNS) codes and full Navier-Stokes (NS) codes were surveyed. PNS techniques can be applied to both the invicid outer flow as well as the viscous inner flow. Although such methods are still not

applicable to flow with strong interaction effects such as separation, they are ideal analytical tools for their efficiency and modest computer requirements. For shear layer driven, strong shock-boundary layer interaction flows, full Navier-Stokes analyses are required.

A correct description of the turbulence structure, which includes the variable density efforts, is the most important feature of the aero-optics flow field analysis. Current state-of-the-art in turbulence modeling cannot generate accurate predictions under general conditions. What can be expected is that satisfactory predictions can be made for categories of flows for parameters of aero-optics concern, even if that requires zonal or ad hoc modeling modifications, so long as the model predictions are verified as acceptable. Thus, by surveying these CFD codes, advances in turbulent fluctuation predictions, compressibility, and turbulence/chemistry coupling can be recommended.

### Technical Results

For the CFD codes identified, a systematic summary of characteristics in terms of numerics, physical models (turbulence models and chemistry models) and validation has been generated. For many CFD codes, a sequential development in terms of numerics upgrades and thermo-physical model upgraded can be identified. In such cases, hierachial characterization approaches are also used. This summary is directly communicated as input to the Data Base.

To gain some confidence in using CFD codes, validations or calibrations of the codes against benchmark experimental data are necessary to examine the accuracy of the physical and numerical models, as well as to highlight the procedures to obtain reliable results. Due to the lack of a sufficiently detailed data base describing various flow processes for a hypersonic flight vehicle, several "unit problems" that delineate dominant physical phenomena applicable for specific components and portions of aero-optics flows are identified. These include: supersonic mixing layer, cavity flows, wall jets and shock/boundary layer interaction. Comparison calculations using different codes versus available experimental data or among various CFD results are then made. Code to code comparisons help quantify numerical errors between algorithms when identical physical models are solved with different methods. The series of validation calculations on chosen unit problems in terms of accuracy and efficiency are also summarized as inputs to the Data Base.

### Important Findings and Conclusion

In examining features of these CFD codes, it can be found that each code assumes some degree of physical or numerical approximations. Numerically, most codes are equipped with shock capturing capabilities by using flux-splitting, TVD or some dissipation schemes. Most codes also use the so-called density-based method in which the governing equations are solved in a coupled fashion. However, a majority of these codes assume that

the flow obeys a perfect gas law and also assume calorically perfect thermodynamics. Only a limited number consider the effects of air chemistry on the gas properties. However, the typical flow environment is such that ideal gas assumptions cannot be applied without careful consideration of the flight envelope and the specific geometry.

The major shortcomings of the most of these codes are the turbulence models used in CFD predictions. Turbulence in aero-optics flows calls for predictions requirements for both the mean flow and fluctuating velocity and density field. All the codes use one-point closure methods which include algebraic models and one, as well as two equation models. Turbulence/chemistry interactions are not accounted for in all codes. Unsteady effects are also not modeled properly.

To conclude, application of CFD methods to analyze aero-optics flows is a powerful tool for supplementing and extending traditional design methods. However, the proper use of CFD requires a systematic application methodology that uses existing codes where possible and includes improved numerics and physical models where dictated by the geometry and flow regimes under consideration. These codes should then be exercised using a series of validation calculations on appropriately chosen unit problems to determine the applicability, accuracy and efficiency of the code.

<u>NAME</u>	<u>SOURCE</u>	<u>DESCRIPTION</u>
1. AFWAL.	NASA Ames	3D PNS code uses Schiff-Steger scheme. Frozen chemistry with an algebraic Baldwin-Lomax turbulence model
2. AIR3D	NASA Ames	3D Navier-Stokes code uses Beam-Warming scheme. Baldwin-Lomax turbulence model for turbulent flow and frozen chemistry.
3. ALMA	U. C. Ervine/Phys. Res. Inc.	2D/Axysymmetric thin-layer Navier-Stokes Code. Utilize Pantankar-Spalding's SIMPLE Algorithm. k- $\epsilon$ model.
4. ARC	NASA-Ames	2D and 3D Navier-Stokes Code with also thin-layer boundary layer form. Use Beam-Warming Scheme and algebraic Baldwin-Lomax for airfoil flow calculations.
5. ARICC	NASA-Marshall	2D multiphase code solves N-S/VOF gas-liquid flow equations using ALE-ICE scheme. Equilibrium and finite-rate chemistry are included for low-speed flow simulation.
6. CFL3D	NASA Langley	3D N-S code uses Beam-Warning scheme for solving high Mach number airfoil flows with significant real gas effects.
7. CNS	NASA-Ames	This code incorporates a partially flux-split algorithm, B-L turbulence model and finite rate chemistry with nonideal gas behavior for the thin-layer, time-dependent Reynolds-averaged N-S equations for hypersonic flows.
8. FDNS	NASA Marshall	2D and 3D N-S code uses SIMPLEC scheme and point-wise implicit solver. Two-equation model and equilibrium chemistry are included for low to supersonic flow calculations.
9. GASP	VPI	3D N-S finite volume code has a generalized finite-rate chemistry algorithm with Steger-Warming, Van Leer, and Roe characteristic-based flux splitting for solving hypersonic blunt body flows.
10. KIVA	Los Alamos	3D N-S code utilized ALE-ICE scheme for multiphase combustion flows of internal combustion engines.
11. MAST	NASA-Marshall	A 2D and 3D N-S code uses multi-step pressure with 2-equation and algebraic stress model for all speed flow simulation. Lagrangian particle tracking capability is included.
12. NASCRIN	NASA Langley	2D and 3D N-S code use MacCormack explicit scheme and Baldwin-Lomax

- turbulence model for hypersonic flow calculations.
13. NASTRAN UTPRC 3D N-S code based on pressure-correction schemes has two-equation model, equilibrium chemistry, finite rate chemistry for low and high speed flow calculations.
  14. NAVIER 7 Rutgers U. 2D and 3D N-S code use MacCormack implicit and explicit schemes for supersonic shock/turbulence B-L calculations. Baldwin-Lomax model and frozen chemistry are used.
  15. NS3D Sandia NL The unsteady thin-layer Navier-Stokes equations are solved with a linearized block ADI finite difference procedure for supersonic external flows.
  16. PANSWIC SAIC Spatial Marching of 3D-PNS equations with alg. or k- $\epsilon$  model for supersonic and hypersonic flows.
  17. PARC AEDC 2D and 3D N-S code use Beam and Warming scheme and utilizes algebraic and k- $\epsilon$  models for transonic, supersonic and hypersonic flows.
  18. PARCII SAIC 2D and 3D N-S code uses Roe-TVD scheme for supersonic and hypersonic calculations. Turbulence are handled by algebraic and k- $\epsilon$  model. Equilibrium and finite rate chemistry are available.
  19. RPLUS NASA Lewis A 2D and 3D full N-S code uses flux splitting scheme and LU fast matrix inversion technique for finite rate chemistry, hypersonic flow calculations.
  20. SCHINOZ SAIC 2D PNS code use MacCormack explicit scheme and k- $\omega$  model in connection with equilibrium/finite rate chemistry for nozzle flows.
  21. SCRAMP SAIC 2D PNS code uses Schiff-Steger scheme and B-L, k- $\epsilon$  models for hypersonic flat plate/compression corner flows. Chemistry is frozen.
  22. SPARK NASA Langley 2D and 3D code uses MacCormack and Baldwin-Lomax model for Ramjet/Scramjet combustor flow field and hypersonic flows. Finite rate chemistry is emphasized.
  23. STURF Penn State U. Thin Layer PNS (2D) code used Chakravarthy-Osher TVD scheme for hyperbolic flow calculations. Finite rate chemistry is strongly coupled with the flow solver.
  24. TONIC NASA Ames Thin-layer PNS code uses Beam-Warning scheme for calculating hypersonic flows. Finite rate chemistry is loosely coupled with the flow solver.

- |     |      |           |  |
|-----|------|-----------|--|
| 25. | UDRI | U. Dayton | A 3D PNS code uses explicit MacCormack scheme and Thomas' shock-fitting scheme for finite rate chemical reacting hypersonic flows.             |
| 26. | UPS  | NASA Ames | 3D PNS code uses Chakravarthy and Szema's upwind TVD scheme for hypersonic flow calculations. Finite rate is loosely coupled with flow solver. |
| 27. | VRA  | VRA       | A PNS code uses fully implicit, crossflow coupled shock-fitting and finite rate chemistry to solve hypersonic external flows.                  |

## Non-Intrusive Measurement Techniques

by

J. E. Smith, Jr.

### Objective

The objective of this phase of the program is to explore and/or develop non-intrusive measurement techniques under high speed flow conditions to characterize wall jet and mixing layer phenomena which influence the quality of aero-optic measurements.

### Approach

The basic approach consists of two principal elements as follows:

- ( i) Develop a computer controlled experimental apparatus to perform short duration wall jet experiments.
- (ii) Examine the flowing stream(s) with various non-intrusive measurement techniques to evaluate local speciation and velocity. Initially, we will investigate the use of chemical tracers and Raman Spectroscopy conducted over fiber optics to determine local speciation within the wall jet.

### Status

A schematic of the flow system is given in the accompanying figure. Relative to that sketch, the brief status is as follows:

- Pressure supply system, vacuum system and scrubber are 90% complete.
- The test section is under design.
- Spectroscopic unit is 75% complete.
- The LDV unit will require software and hardware upgrades to make it fully compatible with the existing data acquisition and computer equipment.

### Future Plans

These plans include the following elements:

- Complete construction of flow system and sub-systems.
- Complete CAD design of the test section and manufacture the design using a computer driven milling machine available at the university.
- Conduct Raman Scattering experiments to measure the local concentration of a chemical tracer added to the wall jet.
- Upgrade the LDV unit to evaluate hybrid system to measure local velocities with LDV and concentrations with Raman Spectroscopy.

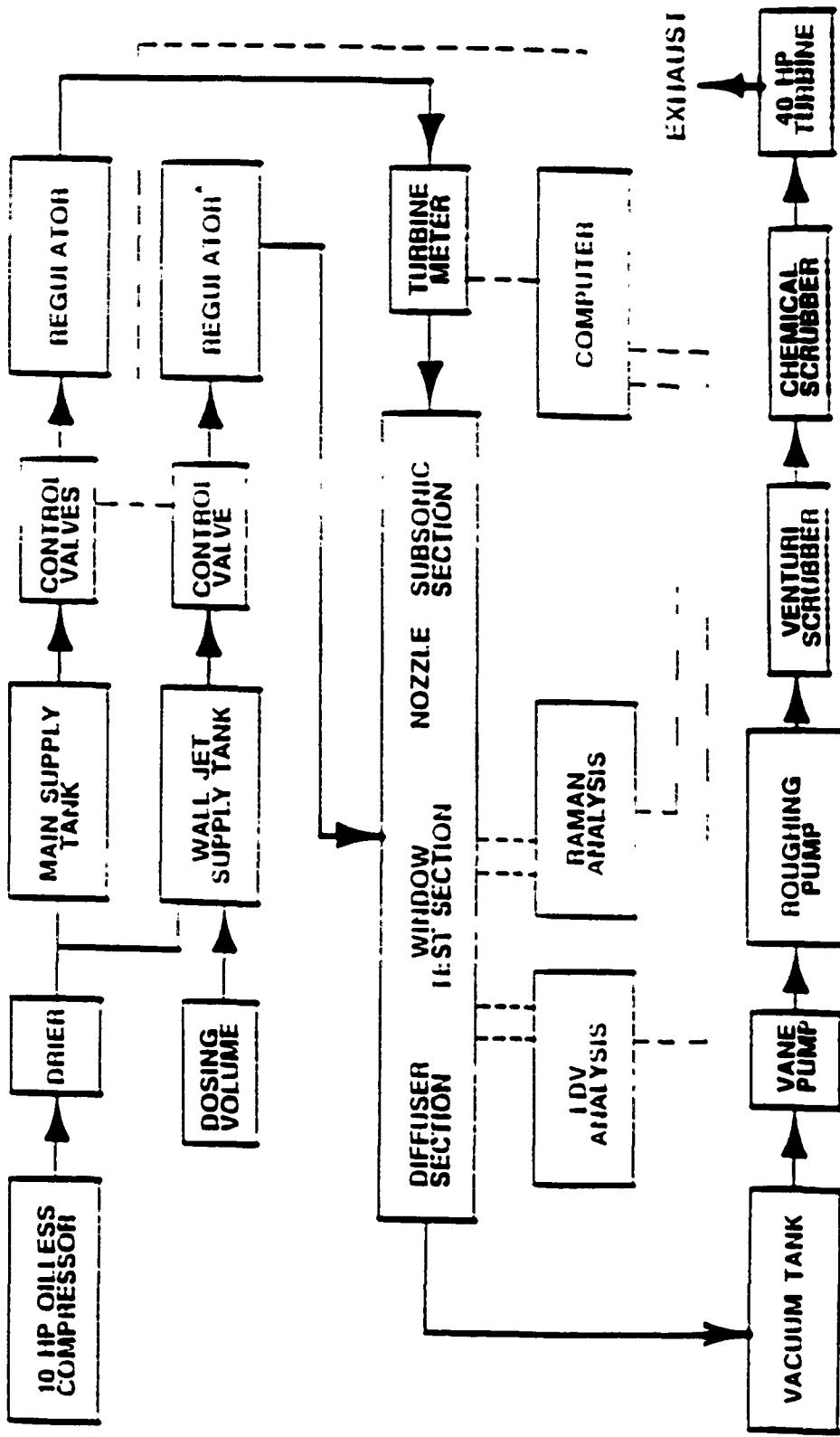


NON-INTRUSIVE MEASUREMENT TECHNIQUES



The University  
Of Alabama  
In Huntsville

## FLOW DIAGRAM FOR THE MACI 2.3 BLOW-DOWN TUNNEL WITH PARTICULATE AND CHEMICAL SCRUBBER - UNDER DEVELOPMENT TO TEST NON-INTRUSIVE MEASUREMENT TECHNIQUES.





## NON-INTRUSIVE MEASUREMENT TECHNIQUES



### DEVELOPMENT OF NON-INTRUSIVE MEASUREMENT TECHNIQUES APPLICABLE TO THE WINDOW COOLING PROBLEM

OBJECTIVES	APPROACH	PLANS
<p>EXPLORATION AND DEVELOP NON INTRUSIVE MEASUREMENT TECHNIQUES UNDER HIGH SPEED FLOW CONDITIONS TO CHARACTERIZE WALL JET AND MIXING LAYER PHENOMENA WHICH INFLUENCE THE QUALITY OF AERO OPTIC MEASUREMENTS</p>	<ul style="list-style-type: none"><li>● DEVELOP A COMPUTER CONTROLLED EXPERIMENTAL APPARATUS TO PERFORM SHORT DURATION WALL JET EXPERIMENTS</li><li>● EXAMINE THE LOCAL STREAM(S) WITH VARIOUS NON INTRUSIVE MEASUREMENT TECHNIQUES TO EVALUATE LOCAL SPECIATION AND VELOCITY. INITIALLY WE WILL INVESTIGATE THE USE OF CHEMICAL TRACERS AND RAMAN SPECTROSCOPY CONDUCTED OVER FIBER OPTICS TO DETERMINE LOCAL SPECIATION WITHIN THE WALL JET.</li></ul>	<ul style="list-style-type: none"><li>● COMPLETE CONSTRUCTION OF FLOW SYSTEM AND SUB SYSTEMS.</li><li>● COMPLETE CAD DESIGN OF THE TEST SECTION AND MANUFACTURE THE DESIGN USING A COMPUTER DRIVEN MILLING MACHINE AVAILABLE AT THE UNIVERSITY</li><li>● CONDUCT RAMAN SCATTERING EXPERIMENTS TO MEASURE THE LOCAL CONCENTRATION OF A CHEMICAL TRACER ADDED TO THE WALL JET.</li><li>● UPGRADE THE LDV UNIT TO EVALUATE HYBRID SYSTEM TO MEASURE LOCAL VELOCITIES WITH LDV AND CONCENTRATIONS WITH RAMAN SPECTROSCOPY</li></ul>
<p>PRESSURE SUPPLY SYSTEM, VACUUM SYSTEM AND SCRUBBER ARE 90% COMPLETE.</p> <p>THE TEST SECTION IS UNDER DESIGN.</p> <p>SPECIROSCOPIC UNIT IS 75% COMPLETE.</p>		<p>THE LDV UNIT WILL REQUIRE SOFTWARE AND HARDWARE UPGRADES TO MAKE IT FULLY COMPATIBLE WITH THE EXISTING DATA ACQUISITION AND COMPUTER EQUIPMENT.</p>

UAH Aero-Optics Data Base

by

J. Ziebarth and S. Graves

Objective

The basic objective is to develop a computerized data management system that will house aerodynamic data related to optics and optics data related to aerodynamics.

Approach

In order to accomplish this task, the fundamental approach is given as follows:

- Integrate a DBMS and a menu driven interface system, to provide a user friendly AODB which is flexible and extendible.
- Include analytical/experimental data, visualization/analysis tools, bibliographical information.
- Maintain compatibility with USASDC-KDEC.

Status

The prototype data base is complete and contains representative data to demonstrate functionality. Moreover, a Configuration Board has been established to direct the selection criteria and management of data.

Future Plans

These plans consist of four key elements as follows:

- ( i) Expand capability as required by users.
- ( ii) Acquire HW/SW for a fully operational AODB.
- ( iii) Provide for acquisition of existing and future data.
- ( iv) Establish connectivity between UAH-AODB and USASDC-KDEC.

Optical Measurement Techniques  
for  
Turbulent Flow Fields

by

M. Abushagur

The turbulent flow in front of the window of an interceptor consists of a medium with variable density and in turn with variable index of refraction. A light beam wavefront traveling through this medium suffers a phase change that deforms the incoming wavefront. The deformation of the wavefront affects the quality of the image observed through this medium. The poor quality of the image of the target effects the tracking capability of the interceptor. Overcoming such a problem requires a knowledge of the flow field density distribution in front of the window. This density distribution can be used to compute the transfer function of the turbulent medium. The transfer function then can be used in designing the proper imaging enhancement system.

Overcoming such a problem requires a knowledge of the flow field density distribution in front of the window. This density distribution can be used to compute the transfer function of the turbulent medium. The transfer function then can be used in designing the proper imaging enhancement system.

Measuring the density distribution without perturbing the flow is a very critical issue in this process. Optical, non-intrusive methods are adequate to such measurements. These techniques are based on the fact that the wavefront of the light beam, as it passes through the turbulent medium, is modulated by the index of refraction distribution. When extracted, this information can be used in mapping the density distribution of the flow field.

There are a number of optical methods which can be used for mapping the flow field. Among these methods are: interferometry, holographic interferometry, speckle photography, shadowgraphs, Schlieren technique, and Moire deflectometry. These methods are not equivalent, each has its own advantages in measuring a certain quantity of the flow field; they also differ very significantly in their complexity. The method we are interested in using in this preliminary stage of our study is Moire deflectometry, which is very powerful in mapping phase objects such as the case for flow fields.

(a) TASK OBJECTIVES

The objective of this work will be to develop optical techniques to reconstruct the flow field distribution in front of the interceptor window. To achieve this objective, a number of simpler tasks are set to develop the measurement techniques.

These subtasks are as follows:

1. Develop non-intrusive optical methods for measuring simple flow fields which are known and for which theoretical models have been developed such as: the temperature distribution in a flame; temperature field around a heated wire; two heated wires, ... etc.
2. Develop the software capable for interpreting the optical data collected from the experiments in terms of flow field distribution plots.
3. Test the algorithms developed in subtask (2) for the measurement of the flow fields of the models mentioned in subtask (1).
4. Build a system (both hardware and software) capable of measuring flow field distribution automatically, i.e. collecting data, analyzing it, and plotting the flow field distribution.

(b) TECHNICAL PROBLEMS

The flow field distribution measurement in front of the interceptor's window is not feasible practically. Wind tunnel measurements are the closest to the real life situation. At this stage of this research, we are considering more fundamental problems, namely, the measurement of a symmetric flow field distribution, an asymmetric flow and finally, a mixing-layer flow field.

(c) GENERAL METHODOLOGY

The Moire effect denotes a fringe pattern formed by the superposition of two grid structures of similar period with some inclination angle as shown in Fig. 1. This method is used in many applications. Yet another more powerful technique for the class of problems we are considering is Moire deflectometry. In the classical Moire fringes, the two gratings are superimposed on one another. On the other hand, in Moire deflectometry, the two grating are placed apart. In this technique, the deformation of the Moire pattern is caused by the ray deflections due to their passage through the phase object (e.g. flows fields). In this technique, the object to be tested is placed in the path of a collimated beam followed by a pair of transmission gratings (Ronchi rulings) placed at a distance from each other as shown in Fig. 2. The Moire deflectogram (the resulting fringe pattern) is a map of ray deflection corresponding to the optical properties (index of refraction distribution) of the test object.

The Moire fringe pattern is produced by crossing two Ronchi rulings as shown in Fig. 1. The fringe spacing depends on the angle  $\theta$ .

$$p^1 = \frac{p}{\sin\theta} \quad (1)$$

where  $p$  and  $p^1$  are the pitches of the Ronchi ruling and Moire fringe spacing, respectively. These fringes can be seen by illuminating the Ronchi ruling with a coherent plane wave. Due to the Talbot effect, these fringes can be seen at periodic distances.

If the plane wave is obstructed with an object that has a variable optical pathlength (optical pathlength is the product of the object thickness and its index of refraction) the fringes no longer are straight. The shape of the produced fringes depends on the index of refraction distribution. As shown in Fig. 3, when a light ray passes through the phase object, because of the index of refraction, it gets refracted (bent) with an angle  $d$ . This angle is related to the index of refraction by the following equation:

$$d(y) = \frac{1}{N_0} \int_{-\infty}^{\infty} \left| \frac{\partial n(x,y,z)}{\partial x^1} \right| dx^1 \quad (2)$$

where  $N_0$  is the index of refraction of the outside medium, and  $\partial/\partial x^1$  is the partial derivative with respect to  $x^1$ .

Let

$$N(Y, X) = n(x, y, z) - N_0, \quad (3)$$

Then  $N(Y, X)$  can be shown to be

$$N(Y, X) = \frac{1}{2\pi^2} \int_{-\pi/2}^{\pi/2} d\theta \int_{-\infty}^{\infty} \frac{d(y^1)}{r \sin(x-\theta) - y^1} dy^1. \quad (4)$$

Hence, the index of refraction distribution  $N(r, x)$  can be computed from Eq. (4) using  $d(y^1)$  data. The deflection angle distribution  $d(y^1, z)$  can be determined from the intensity distribution,  $I(y, z)$ , of Moire deflectogram from the following relation.

$$d(y^1, z) = m\pi I(y^1, z) + 2k\pi; \quad (5)$$

where  $m = I1$  and  $k = 0, I1, I2, \dots$

The values for  $m$  and  $k$  can be determined by a set rules. After determining the deflection angle distribution, the index of refraction distribution can be calculated from the inverse of the Abel's transform, Eq. (4).

#### (d) TECHNICAL RESULTS

An experiment was performed at UAH ECE labs for measuring the temperature distribution across a flame. The setup used is shown in Fig. 4. A HeNe laser was used to illuminate a candle flame; the light is then passes through two Ronchi rulings spaced at their first periodic distance. A photodiode was used to measure

the light intensity across the Moire deflectogram. The intensity distribution is plotted in Fig. 5 as a function of the distance across the deflectogram. This intensity distribution data was then used to determine  $d(y^1, z)$  in Eq. (5). The deflection angle computed is plotted in Fig. 6. The data from the deflection angle is substituted in Eq. (4) to determine the inverse Abel's transform to compute the index of refraction distribution through the flame; this distribution is inversely proportional to the temperature distribution. The temperature distribution which results from these calculations is shown in Fig. 7.

The resultant temperature distribution across the flame is a good representation and agrees with theoretical and direct measurements.

(e) IMPORTANT FINDINGS

The Moire deflectometry method, used in this stage of research for the flow field distribution measurement, was used to determine the flow field (tempereration distribution) of a flame. Results were very encouraging. This method, in the future, will be extended to different objects as outlined previously in section (a) of this report.

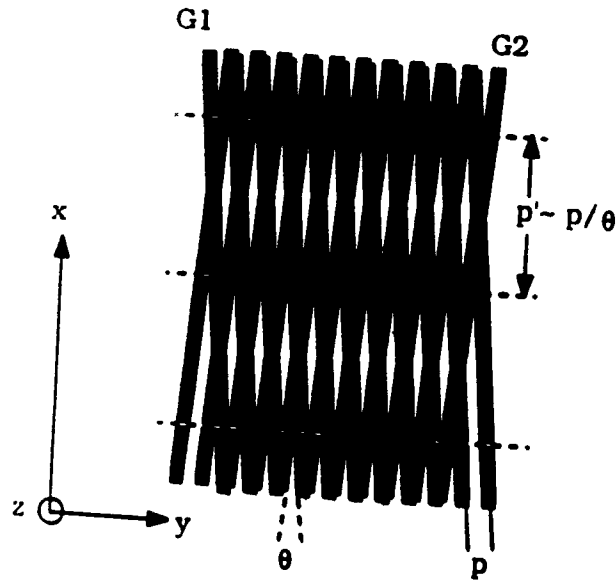


**Figure 1**

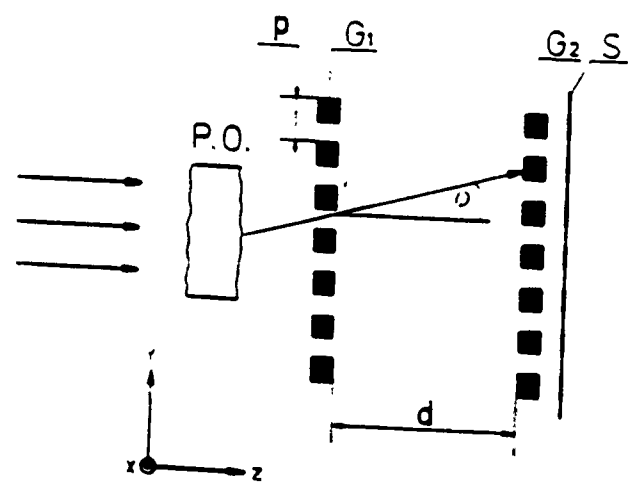


**Figure 2**

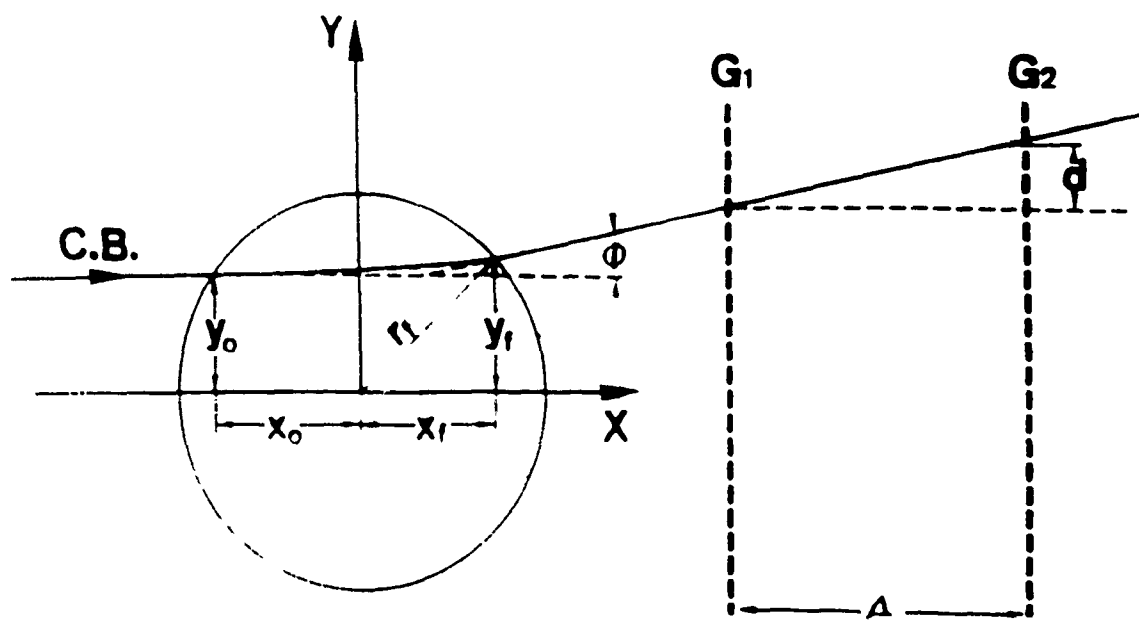


Figure 3

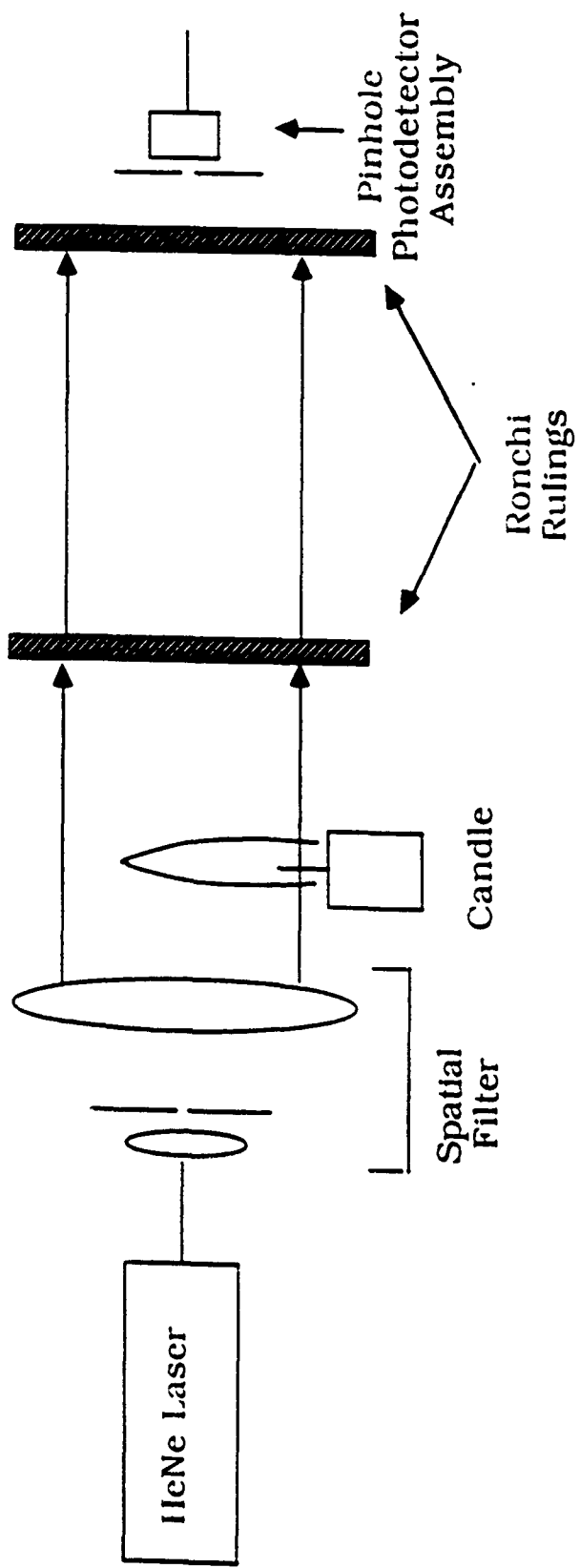


Figure 4

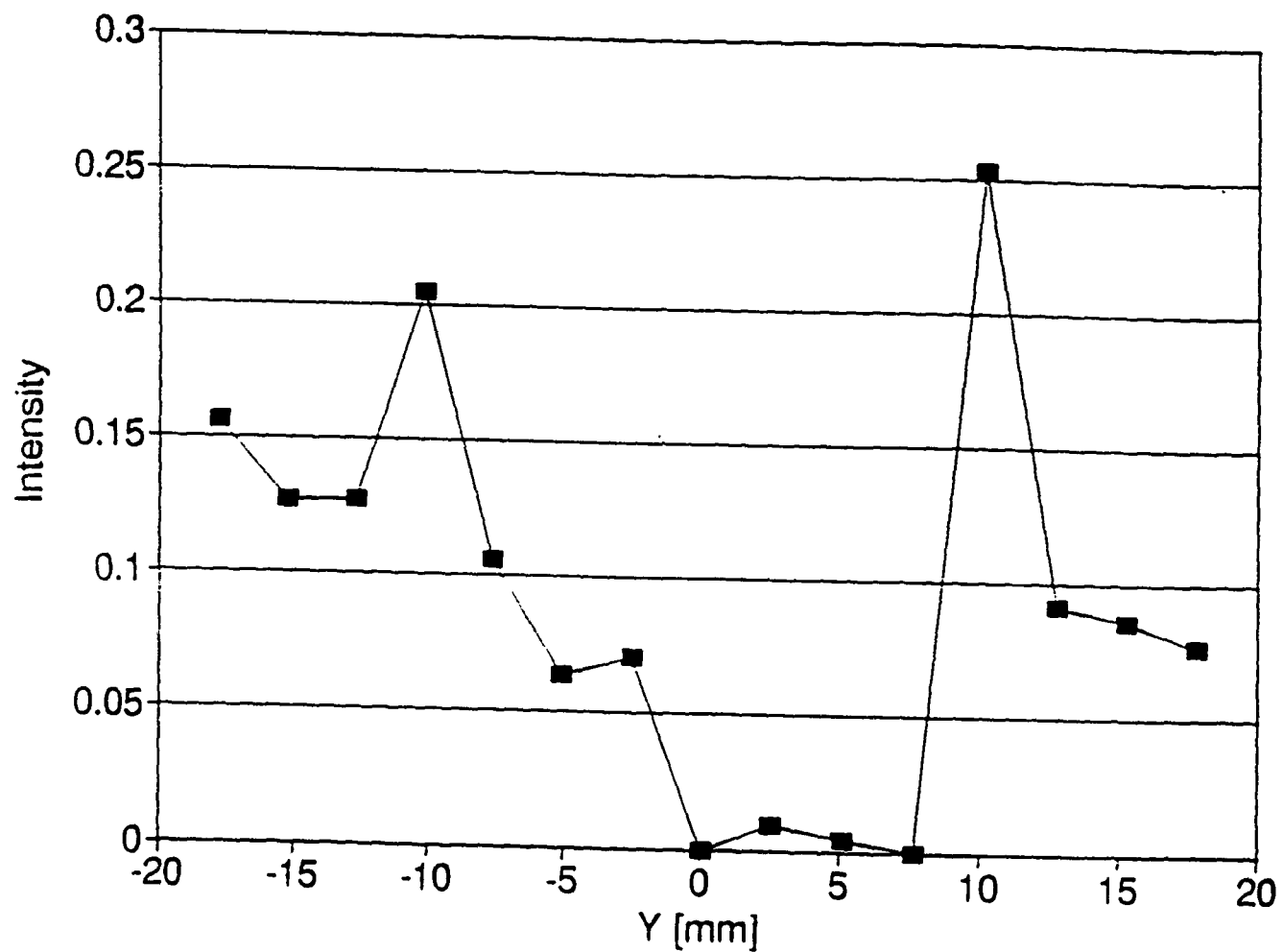
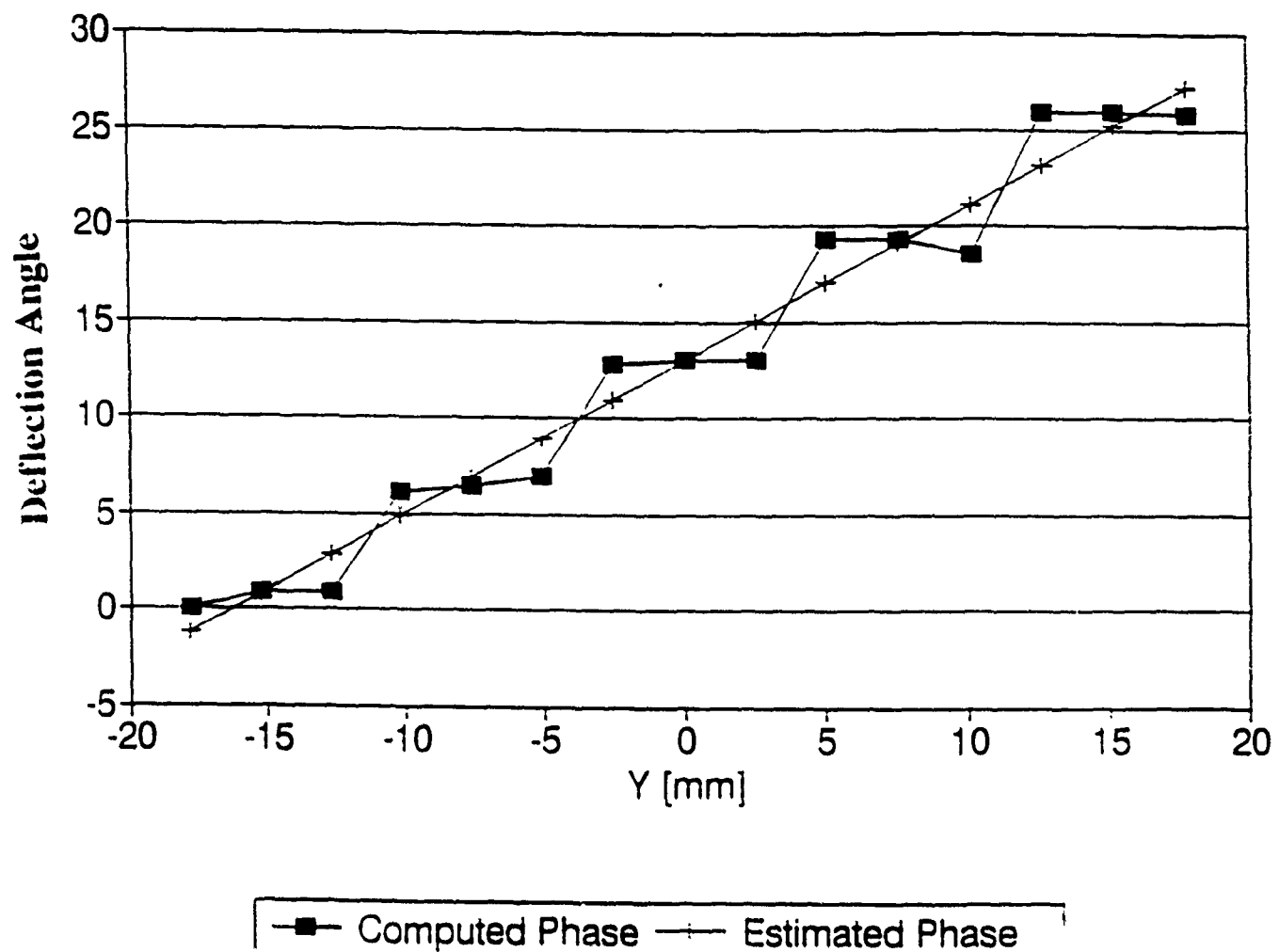


Figure 5



**Figure 6**

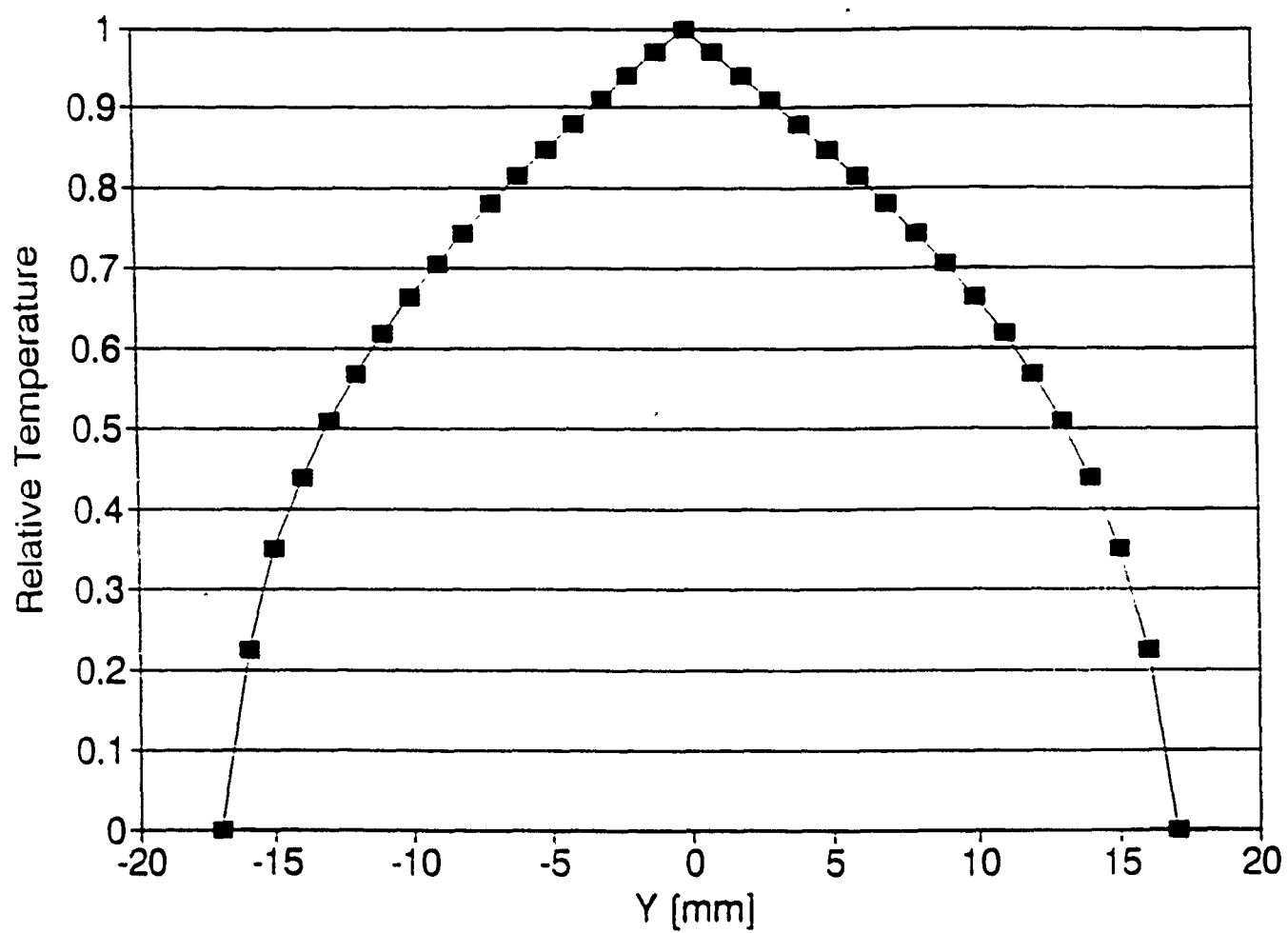


Figure 7

# Image Restoration by Least-Squares (Wiener) Filter

*By*

*Kyeong-Seop Kim*

*Ph.D. Student, ECE Department*

Electrical and Computer Engineering Department

University of Alabama in Huntsville. Huntsville. Alabama 35899

## PREFACE

This document is a report on restoring image which is blurred by Aero-Optics effects via Least-Squares (Wiener) Filter. The goal of this research is to develope a digital filter algorithm for estimating the ideal image from the blurred image using *a posteriori* information. Technical work was accomplished by Mr. Kyeong-Seop Kim, a graduate student in the ECE Department, under the supervision of Dr. Reza Adhami.

# **Contents**

<b>1</b>	<b>Introduction</b>	<b>3</b>
<b>2</b>	<b>Models for Blurred Image Formation</b>	<b>4</b>
2.1	Image Formation . . . . .	4
2.2	Image Model . . . . .	6
2.3	Blur Models . . . . .	7
<b>3</b>	<b>Parametric Blur Identification</b>	<b>8</b>
<b>4</b>	<b>Wiener filter for restoring blurred image</b>	<b>9</b>
4.1	Inverse Filter for Image Restoration . . . . .	9
4.2	Wiener Filter for Image Restoration . . . . .	10
<b>5</b>	<b>Experiments and Results</b>	<b>12</b>
5.1	Data Acquisition . . . . .	12
5.2	Contrast Manipulation . . . . .	14
5.3	Image Restoraton by Global Image Statistics . . . . .	15
5.3.1	Blur Identification . . . . .	15

5.3.2	Image Restoration . . . . .	16
5.4	Image Restoration by Local Image Stastistics . . . . .	18
5.4.1	Blur Identification . . . . .	18
5.4.2	Image Restoration . . . . .	21
5.5	Conclusion . . . . .	24

# 1 Introduction

Images are produced to record or display useful information, but the process of image formation and recording is imperfect. The recorded image invariably represents a degraded version of the original scene. Blurring can be caused by relative motion between the camera and the original scene, or by an optical system that is out of focus. When aerial photographs are produced, blurs are introduced by atmospheric turbulence, and relative motion between the camera and the object. An example of such blurring process is the Aero-Optic Mixing/Shear Layer measurements problem. When a hypersonic vehicle is launched, the window in this vehicle must be cooled. Unfortunately, the mixing/shear layer formed between the environment gas and the coolant gas causes severe optical degradation. Thus we need to restore or estimate the original scene from this degraded one by gas turbulence. The field of image restoration is concerned with the reconstruction or estimation of an uncorrupted image from a distorted and noisy one. Thus, restoration techniques are oriented toward modeling the degradation and applying the inverse process in order to recover the original image. This report is arranged into several sections. Section 2 discusses mathematical models for images and blur operators. Procedures for deblurring require complete knowledge of the blurring function. As this is rarely available, Section 3 discusses *parametric* blur identification for the estimating of the blurring operator from the blurred image itself. Section 4 discusses the Wiener image restoration filter. The Wiener filter is the optimum filter for minimizing errors between the given degraded image and the estimated ideal image. The data obtained, the experiments performed including *nonparametric* blur identification and Wiener filtered image restoration, and the conclusions

drawn from this research are listed in Section 5.

## 2 Models for Blurred Image Formation

### 2.1 Image Formation

For notational convenience, consistency, and ease of understanding, the following format will be established:

- $g(x, y)$  will be the recorded image;
- $f(x, y)$  will be the ideal image, which is a 2-D mapping of the 3-D input scene;
- $h(x, y; s, t)$  will be the 2-D impulse response (point spread function);
- $s\{\cdot\}$  will be the sensor nonlinearity which will be modeled as a point operator;
- $n(x, y)$  will be 2-D noisy process;

If the image formation process is linear, the recorded image can be modeled as the output of the system shown in *Fig.1*, which is given mathematically by

$$g(x, y) = s \left\{ \int_{-\infty}^{+\infty} \int_{-\infty}^{+\infty} h(x, y; s, t) f(s, t) ds dt \right\} + n(x, y) \quad (1)$$

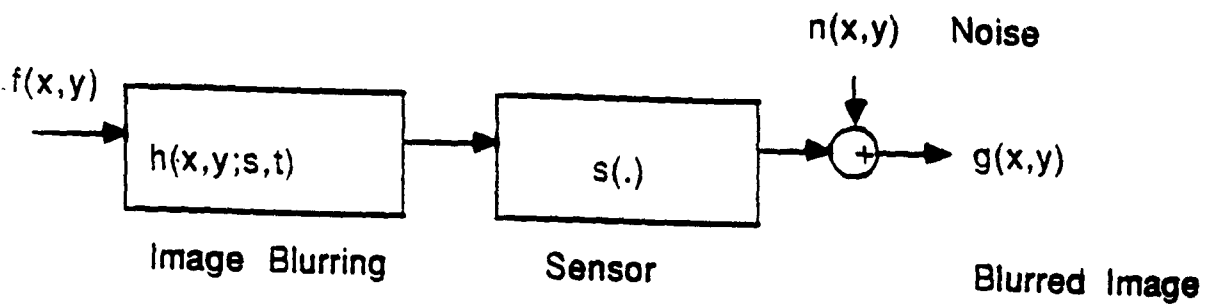


Figure 1: Model for the processes of image formation and recording.

The noise contribution is shown in *Fig.1* as an additive random process which is statistically uncorrelated with the image. If the impulse response is stationary across the image and object fields, it becomes a function of only the argument differences  $x - s$  and  $y - t$ . In this case,

$$g(x, y) = s \left\{ \int_{-\infty}^{+\infty} \int_{-\infty}^{+\infty} h(x - s, y - t) f(s, t) ds dt \right\} + n(x, y) \quad (2)$$

$$g(x, y) = s \{ h(x, y) * f(x, y) \} + n(x, y) \quad (3)$$

where (\*) is used to denote 2-D convolution.

In a discrete implementation, continuous arguments f, g, h and n are replaced by arrays of samples taken on  $N \times N$  2-D rectangular lattices of equi-spaced samples. The sampled arrays are related by

$$g(i, j) = s \left\{ \sum_{k=0}^{N-1} \sum_{l=0}^{N-1} h(i, j; k, l) f(k, l) \right\} + n(i, j) . \quad 0 \leq i, j \leq N - 1 \quad (4)$$

For the spatially invariant (stationary) system, the convolution integral (2) becomes a convolution sum

$$g(i, j) = s \left\{ \sum_{k=0}^{N-1} \sum_{l=0}^{N-1} h(i - k, j - l) f(k, l) \right\} + n(i, j) \quad (5)$$

$$g(i, j) = s \{ h(i, j) * f(i, j) \} + n(i, j) \quad (6)$$

where the asterisk (\*) is now used to denote a discrete convolution. Often the sensor nonlinearity is conveniently neglected (or linearized) to justify the use of a linear restoration filter. When this nonlinearity is ignored, (6) reduces to the linear convolution model

$$g(i, j) = h(i, j) * f(i, j) + n(i, j) \quad (7)$$

for which discrete Fourier transform can be used to yield the frequency domain model

$$G(m, n) = H(m, n)F(m, n) + N(m, n) \quad (8)$$

Here  $H(m, n)$  represents samples of the frequency response of the blurring system and  $m$  and  $n$  are the discrete frequency variables.

## 2.2 Image Model

Certain linear image restoration techniques including Wiener filter make use of *a priori* statistical knowledge of the original (undistorted) image. This takes the form of a power density spectrum for the Wiener filter. A large class of real-world images can be modeled as the following 2-D autoregressive process of low order:

$$f(i, j) = \sum_{(p, q) \in W_1} u(p, q)f(i - p, j - q) + u(i, j) . \quad \forall(i, j) \quad (9)$$

Here  $u(i, j)$  can be viewed as the error in approximating  $f(i, j)$  using a linear combination of neighboring sample values contained in a neighborhood  $W_1$ . Some common choices for  $W_1$  are illustrated in Fig.2. A comprehensive survey of these three image models has been given by [5].

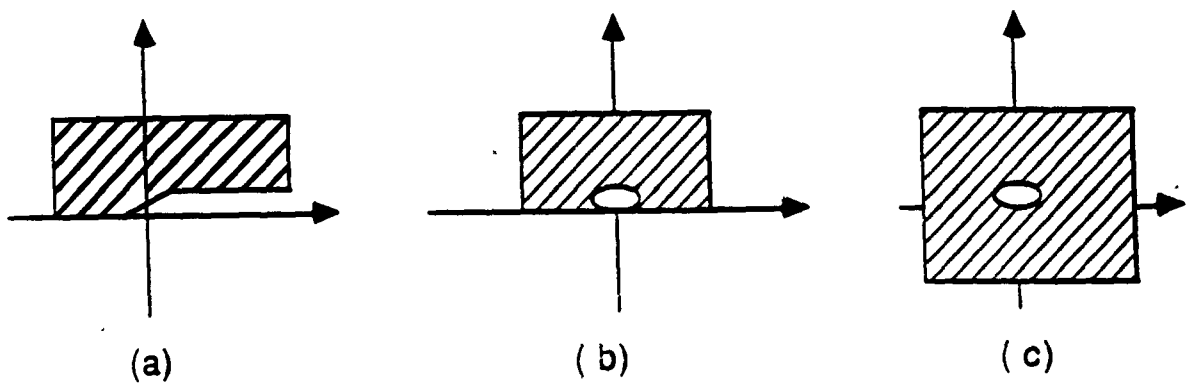


Figure 2: Image model support corresponding to (a) nonsymmetric halfplane:(b) semicausal;(c) noncausal image model.

### 2.3 Blur Models

- Motion Blur: Many types of motion blur are caused by relative motion between the camera and the object. This can be in the form of a translation, a rotation, a sudden change of scale, or some combination of these. For example, when the object translates at a constant horizontal velocity  $V$  during the exposure interval  $[0, T]$ , the distortion is one-dimensional and the discrete point-spread function makes use of the blurring distance  $L$ , which is the number of additional points in the image resulting from a single point in the original scene.

$$h(i, j; k, l) = \frac{1}{(L+1)} \quad , \quad 0 \leq i - k \leq L \quad (10)$$

The frequency response corresponding to this blur is given by

$$H(m, n) = \frac{1}{(L+1)} \exp(-j(\frac{L\pi}{V})m) \frac{\sin(\frac{\pi(L+1)m}{V})}{\sin(\frac{\pi m}{V})} \quad (11)$$

This frequency response shows zero on lines parallel to the  $n$ -axis with an interline spacing of  $\frac{V}{(L+1)}$ . The presence of these parallel zeros in the frequency domain indicates the direction of motion.

- Out-of-Focus Blur: When a three-dimensional scene is imaged by a camera on some parts of the scene are in focus while other parts are not. The degree of defocus depends upon the effective lens diameter and the distance between the object and the camera. The corresponding point spread function is

$$h(x, y) = \frac{1}{\pi r^2} , \quad x^2 + y^2 \leq r^2 \quad (12)$$

where  $r$  is the radius of the circle of confusion. The frequency response  $H(m, n)$  is given by

$$H(m, n) = \frac{J_1(r\rho)}{r\rho} . \quad \rho^2 = m^2 + n^2 \quad (13)$$

where  $J_1$  is the first-order Bessel function.

- Blur due to atmospheric turbulence

$$h(x, y) = C \exp\left\{-\frac{x^2 + y^2}{2\sigma^2}\right\} \quad (14)$$

### 3 Parametric Blur Identification

If the type of degradation is known such as linear motion blur and out-of-focus blur, the blur can be identified by the *parametric* blur description. For linear motion blur, as given in (10) it is only necessary to estimate the direction of blur and the blurring distance. Such a motion blur is often sufficient to estimate the zero patterns in the frequency response from which one can estimate the direction of motion and the blurring distance. With the simplified model for an out-of-focus blur in Eq. (12), it is only necessary to estimate the radius of the circle of

confusion. In this case, the frequency zero patterns can be used to estimate the radius of the circle of confusion.

## 4 Wiener filter for restoring blurred image

### 4.1 Inverse Filter for Image Restoration

Let  $f$ ,  $g$ , and  $n$  represents  $N \times N \times 1$  column vectors formed by stacking the rows of the  $N \times N$   $f(i,j)$ ,  $g(i,j)$ , and  $n(i,j)$ . The first  $N$  elements of  $f$ , for example, are the elements in the first row of  $f(x,y)$ , the next  $N$  elements are from the second row, and so forth for all  $N$  rows of  $f(x,y)$ . Using this convention, Eq. (5) can be expressed in the following vector-matrix form:

$$g = Hf + n \quad (15)$$

where  $H$  is of dimension  $N^2 \times N^2$ . More details for this description are explained in [4]. From Eq. (15), the noise term in the degradation model is given by

$$n = g - Hf \quad (16)$$

In the absence of any knowledge about  $n$ , a meaningful criterion function is to seek an  $\hat{f}$  such that  $H\hat{f}$  approximates  $g$  in a least-squares sense by assuming that the norm of the noise term is as small as possible. In other words, we wish to find an  $\hat{f}$  such that

$$\| n \|^2 = \| g - H\hat{f} \|^2 \quad (17)$$

is minimum. where,  $\| \cdot \|$  is norm operator. From Eq. (17), we may equivalently view this problem as one of minimizing the criterion function

$$J(\hat{f}) = \| g - H\hat{f} \|^2 \quad (18)$$

with respect to  $\hat{f}$ .

Minimization of Eq. (18) can be obtained by simply differentiate  $J$  with respect to  $\hat{f}$ , and set equal to zero, that is.

$$\frac{\partial J(\hat{f})}{\partial \hat{f}} = 0 = -2H'(g - H\hat{f}) \quad (19)$$

Here  $H'$  means the transpose of  $H$ . Solving Eq. (18) for  $\hat{f}$  yields

$$\hat{f} = H^{-1}(H')^{-1}H'g = H^{-1}g \quad (20)$$

## 4.2 Wiener Filter for Image Restoration

Let  $Q$  be a linear operator on  $f$ . In this section we consider the least squares restoration problem as one of minimizing functions of the form  $\| Q\hat{f} \|^2$ , subject to the constraint  $\| g - H\hat{f} \|^2 = \| n \|^2$ . This approach introduces considerable flexibility in the restoration process because it yields different solutions for different choices of  $Q$ . The addition of an equality constraint in the minimization problem can be handled by using the method of Lagrange multipliers. The procedure is to express the constraint in the form  $\alpha(\| g - H\hat{f} \|^2 - \| n \|^2)$  and then append it to the function  $\| Q\hat{f} \|^2$ . In other words, we seek an  $\hat{f}$  which minimizes the criterion function.

$$J(\hat{f}) = \| Q\hat{f} \|^2 + \alpha(\| g - H\hat{f} \|^2 - \| n \|^2) \quad (21)$$

where  $\alpha$  is a constant called the *Lagrange multiplier*. Differentiating Eq. (20) with respect to  $\hat{f}$  and setting the result equal to zero yields the solution  $\hat{f}$ ; that is

$$\hat{f} = (H'H + \gamma Q'Q)^{-1} H'g \quad (22)$$

where  $\gamma = \frac{1}{\alpha}$ .

Let  $R_f$  and  $R_n$  be the correlation matrices of  $f$  and  $n$ , defined respectively by the equations

$$R_f = E\{ff'\}, \quad R_n = E\{nn'\} \quad (23)$$

where  $E\{\cdot\}$  denotes the expected value operation. The ijth element of  $R_f$  is given by  $E\{f_i f_j\}$ , which is the correlation between the  $i$ th and the  $j$ th elements of  $f$ . By defining

$$Q'Q = R_f^{-1}R_n \quad (24)$$

and substituting this expression in Eq. (22) we obtain

$$\hat{f} = (H'H + \gamma R_f^{-1}R_n)^{-1} H'g \quad (25)$$

In frequency domain, Eq. (25) is transformed to

$$\hat{F}(u, v) = \left( \frac{H^*(u, v)}{|H(u, v)|^2 + \gamma \left( \frac{S_n(u, v)}{S_f(u, v)} \right)} \right) G(u, v) \quad (26)$$

for  $u, v = 0, 1, 2, \dots, N-1$ , where  $|H(u, v)|^2 = H^*(u, v)H(u, v)$  and  $S_f(u, v) = F\{R_f\}$ ,  $S_n(u, v) = F\{R_n\}$ . when  $\gamma = 1$ , the term inside the outer brackets in Eq. (26) reduces to the so-called Wiener filter. In the absense of noise ( $S_n(u, v) = 0$ ), the Wiener filter reduces to the ideal inverse filter discussed in the previous section.

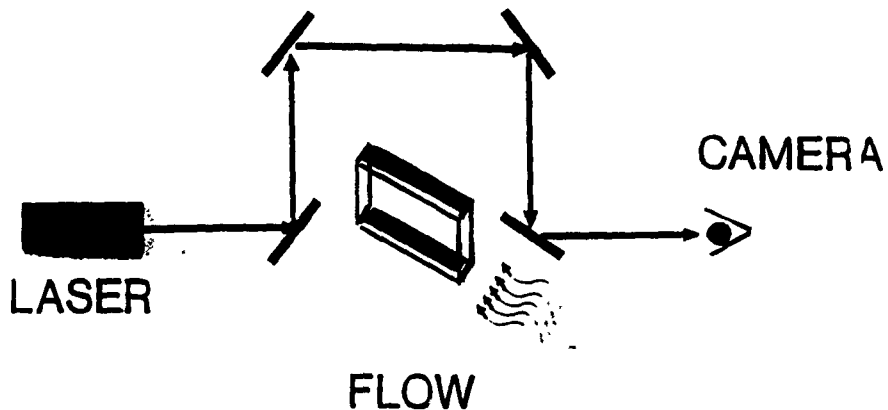


Figure 3: Vibration Detector

When  $S_n(u, v)$  and  $S_f(u, v)$  are not known (a problem often encountered in practice) it is useful to approximate Eq. (26) by the relation

$$\hat{F} \approx \left( \frac{1}{H(u, v)} \frac{|H(u, v)|^2}{|H(u, v)|^2 + K} \right) G(u, v) \quad (27)$$

where  $K$  is constant which is tuned interactively.

## 5 Experiments and Results

### 5.1 Data Acquisition

From Teledyne Brown Engineering Laboratory, we have simulated Aero-Optics images generated from emulating the mixing/shear layer as shown in *Fig.3*. These test images have dimension 128 x 128 (6 bit gray levels) and have two different set. One set of images (128 x 128 x 69 frames) called "tare" were obtained without mixing  $CO_2$  gas flow. One of these images is shown in *Fig.4*. The other set of images called "CO2test" images (128 x 128 x 147 frames) was obtained with mixing simulated environmental and the ~~coolant~~ <sup>coolant</sup>  $CO_2$  gas flow. When the gas flow is flowing on the emulating mixing/shear layer, the impact of flow may generates the vibration and causes the motion blur. Hence we detour the laser beam from the window to

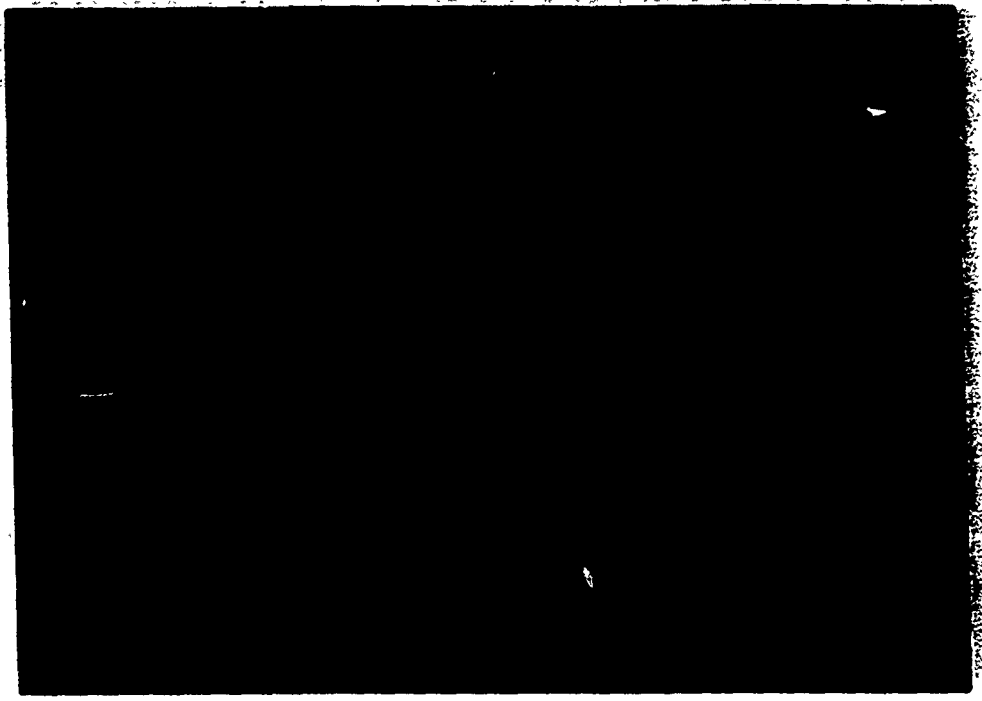


Figure 4: Pseudo Colored Tare Image (Unblurred Image) at First Frame

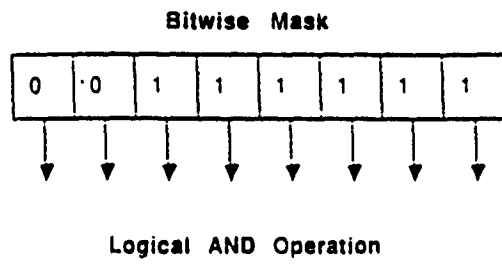


Figure 5: Bitwise Logical AND operator

avoid vibration effects. Since these test images contain 6 bit gray levels, we took logical AND operation with the bitwise mask as shown in *Fig.5*. One of these "Co2test" images is shown in *Fig.6*. The image shown in *Fig.6.* has a very low *contrast*.

*Image contrast* is related to the range of gray levels in an image; the greater the range, the greater the contrast and vice versa. Contrast, C, may be defined numerically in the following way,

$$C = GL_{max} - GL_{min} \quad (28)$$

where  $GL_{max}$  and  $GL_{min}$  are the maximum and minimum gray levels in the image. Normally

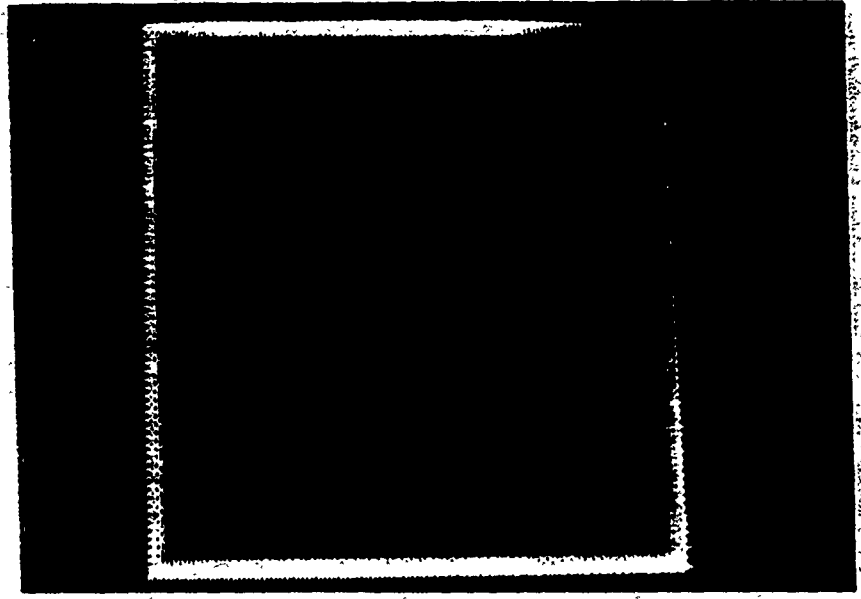


Figure 6: CO2test Image (Blurred Image by CO2 gas at First Frame

$GL_{max} = 255$  and  $GL_{min} = 0$ . Thus image contrast C is 255 (8 bit gray levels) for the most of images. In fact, "Co2test" images have a  $GL_{max} = 10$  and  $GL_{min} = 0$ . Since human eyes can not have a visual discrimination for this low contrast image as shown in Fig.6, one can not see any object in this image. Hence *contrast* manipulation is needed to increase the contrast of a displayed "CO2test" image by expanding the original gray level range to fill the dynamic range of the display device.

## 5.2 Contrast Manipulation

Contrast manipulation is a pixel-by-pixel radiometric transformation that is designed to enhance visual discrimination of low contrast image features. Each pixel's gray level is changed by the specified transformation, without regard for neighboring pixel gray levels. The contrast modification performed in this experiment is *linear* radiometric transformations. This simple linear transformation is routinely used to increase the contrast of a displayed image by expand-

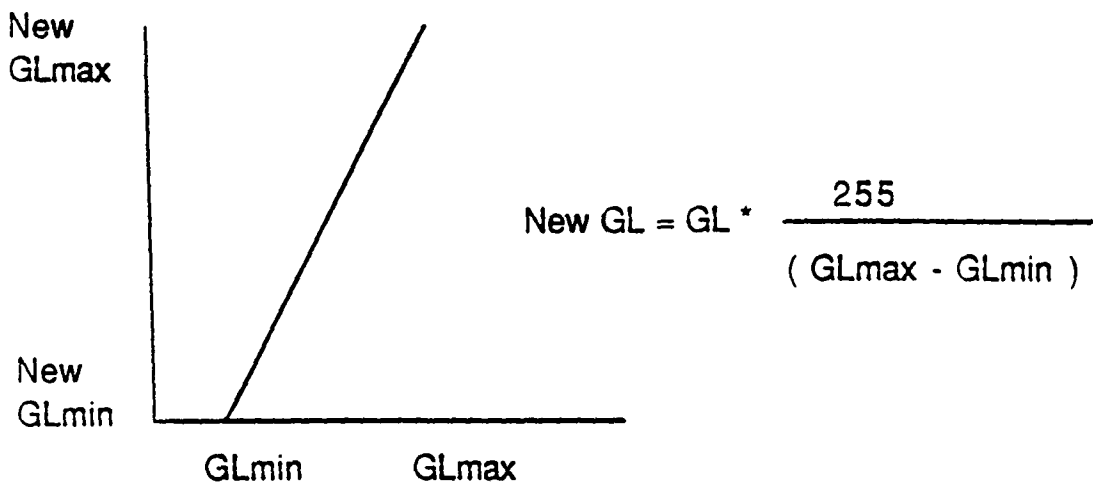


Figure 7: Linear Contrast Stretcher

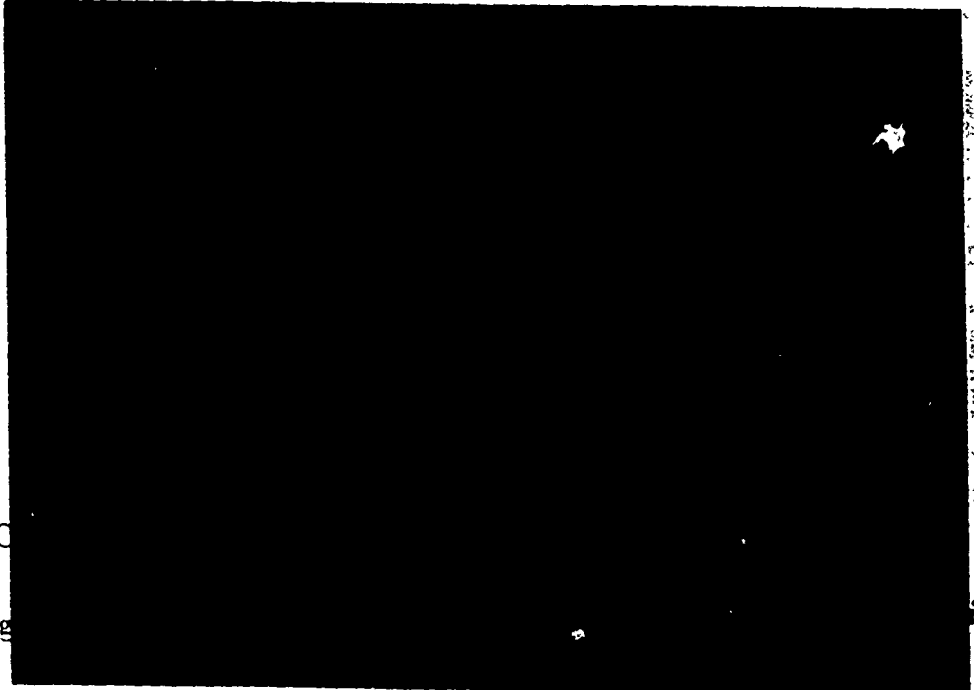


Figure 8: C

ing the original g

Fig.7).

*Fig.8.* shows the contrast stretched image on *Fig.6*.

### 5.3 Image Restoraton by Global Image Statistics

#### 5.3.1 Blur Identification

From Eq. (8),  $H(u,v)$  is related with

$$H(u,v) = \frac{G(u,v) - N(u,v)}{F(u,v)} . \quad 0 \leq u, v \leq 127 \quad (29)$$

Here  $H(u, v)$ ,  $G(u, v)$ ,  $F(u, v)$  and  $N(u, v)$  represents samples of the frequency response of  $h(i, j)$ ,  $g(i, j)$ ,  $f(i, j)$ , and  $n(i, j)$  respectively. By ignoring noise term.

$$H(u, v) \approx \frac{G(u, v)}{F(u, v)} , \quad 0 \leq u, v \leq 127 \quad (30)$$

### 5.3.2 Image Restoration

Since  $N(u, v)$  is  $128 \times 128$  dimension. we can not estimate  $N(u, v)$  globally. Hence we use the approximated Wiener filter by tuning  $K$  value as shown in Eq.(27). Sometimes one can obtain estimates of the noise variance and possible noise power spectrum  $S_n(u, v)$  from relatively smooth local regions in the blurred image  $g(i, j)$ . By selecting  $32 \times 32$  smoothed local region. one can estimate noisy variance  $\sigma^2$  by the following equation.

$$\sigma^2 = \frac{1}{N_n - 1} \sum_{l=0}^{N_n-1} \sum_{k=0}^{N_n-1} (n(l, k) - E\{n(l, k)\})^2 . \quad 0 \leq l, k \leq 31 \quad (31)$$

As suggested by [4]. one can select the tuning factor  $K = 2\sigma^2$ . After Wiener filtered according to Eq. (27) . inverse discrete fourier transformed. and linear contrasted restored image  $\hat{f}(x, y)$  is displayed Fig.9.

For the mulchannel-image case of interest, let  $F(u, v)$ ,  $G_i(u, v)$ , and  $H_i(u, v)$  be the Fourier transformed images of the unblurred, the  $i$ th blurred image, and the  $i$ th point spread function. respectively. According to [3], the Multichannel Wiener filtered image estimate is

$$F_e(u, v) = \frac{\sum_{i=1}^N H_i^*(u, v) G_i(u, v)}{\{\sum_{i=1}^N |H_i(u, v)|^2 + K_{avg}\}} \quad (32)$$

where  $i = 1, 2, \dots, N$  Channels and  $K_{avg} = \frac{\sum_{i=1}^N 2\sigma_i^2}{N}$  with  $\sigma_i$  estimated noise variance of each  $i$  channel image by selecting  $32 \times 32$  local window.

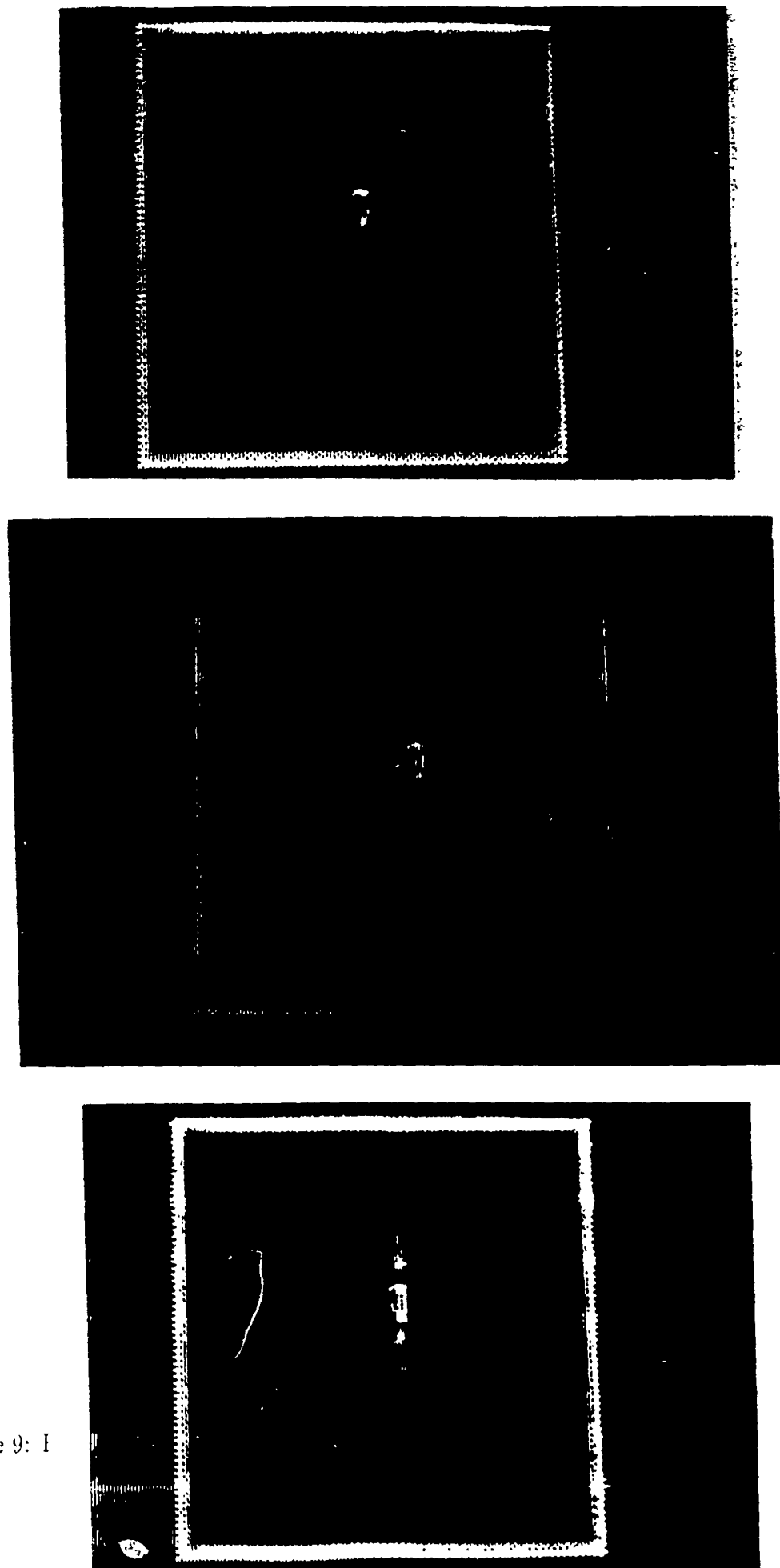


Figure 9: I

) 69th Frame

Having more than one blurred image of a common object provides information that can be used to advantage in the restoration process. One of the advantages is in the area of noise reduction through statistical independence between image noise fields. The second is the potential elimination of zeros in the denominator of the restoration filter [Eq. (27)] by proper selection of the  $H_i(u, v)$ 's or by requiring just one  $H_i(u, v)$  to have noncommon zeros with all other  $H_i(u, v)$ 's. Fig. 10 shows the Multichannel Wiener filter restored and contrast stretched images.

## 5.4 Image Restoration by Local Image Statistics

### 5.4.1 Blur Identification

This blur identification technique is developed by [2]. The degraded image  $g(i, j)$  is divided into subimage  $g_i(i, j)$  which may overlap. If one assumes that the extent of the PSF  $h(i, j)$  is small compared to the extent of the subimage  $g_i(i, j)$  and ignoring the noise term, then, approximately.

$$G_i(u, v) \approx H(u, v)F_i(u, v) \quad (33)$$

According to [2], the magnitude of  $H(u, v)$  is

$$|H(u, v)|^2 = \frac{\frac{1}{N} \sum_{i=1}^N |G_i(u, v)|^2}{\frac{1}{N} \sum_{i=1}^N |F_i(u, v)|^2} \quad (34)$$

where  $i$  is each subimage index and  $N$  is the total number of subimages. In our experiments, we select  $32 \times 32$  subimage with 0 and 50 % overlapping neighborhood subimage respectively.

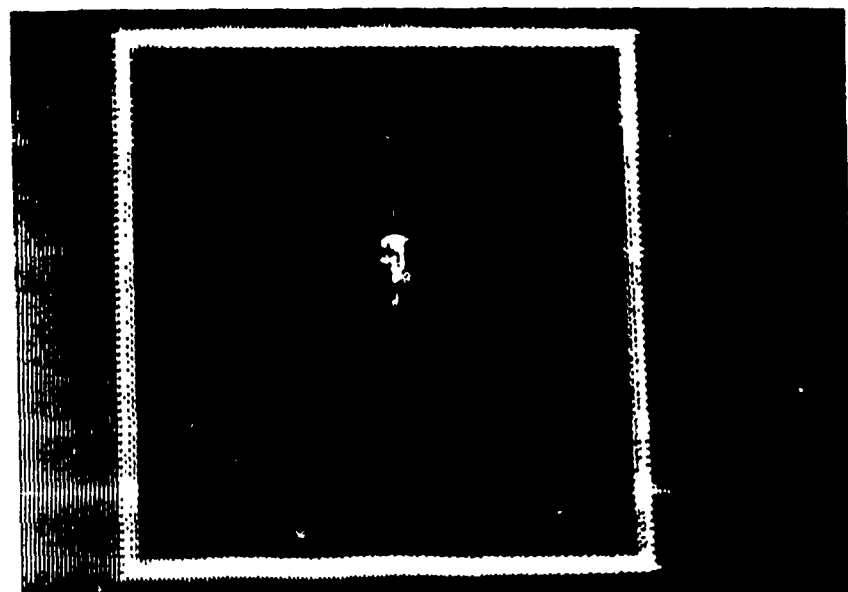
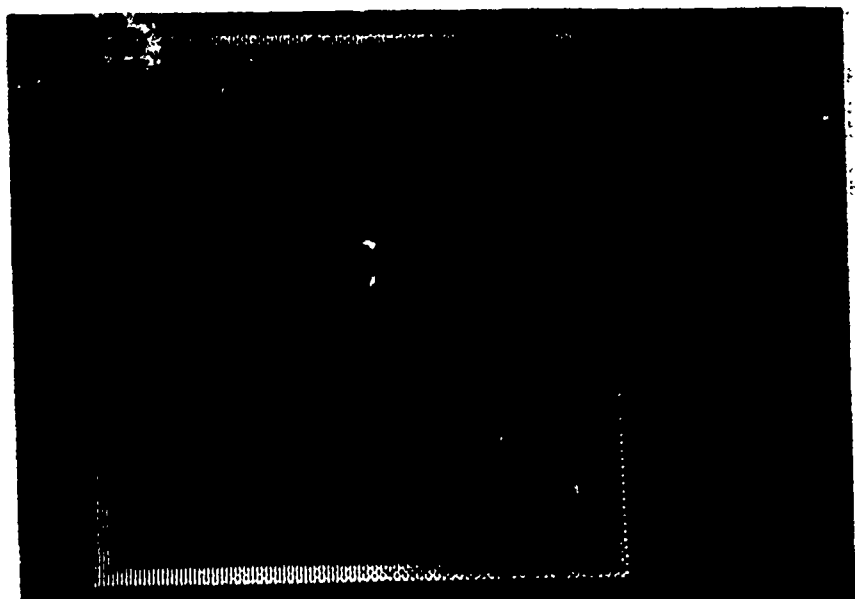


Figure  
68, 69

Figure 1, 32, 69 :c)67,

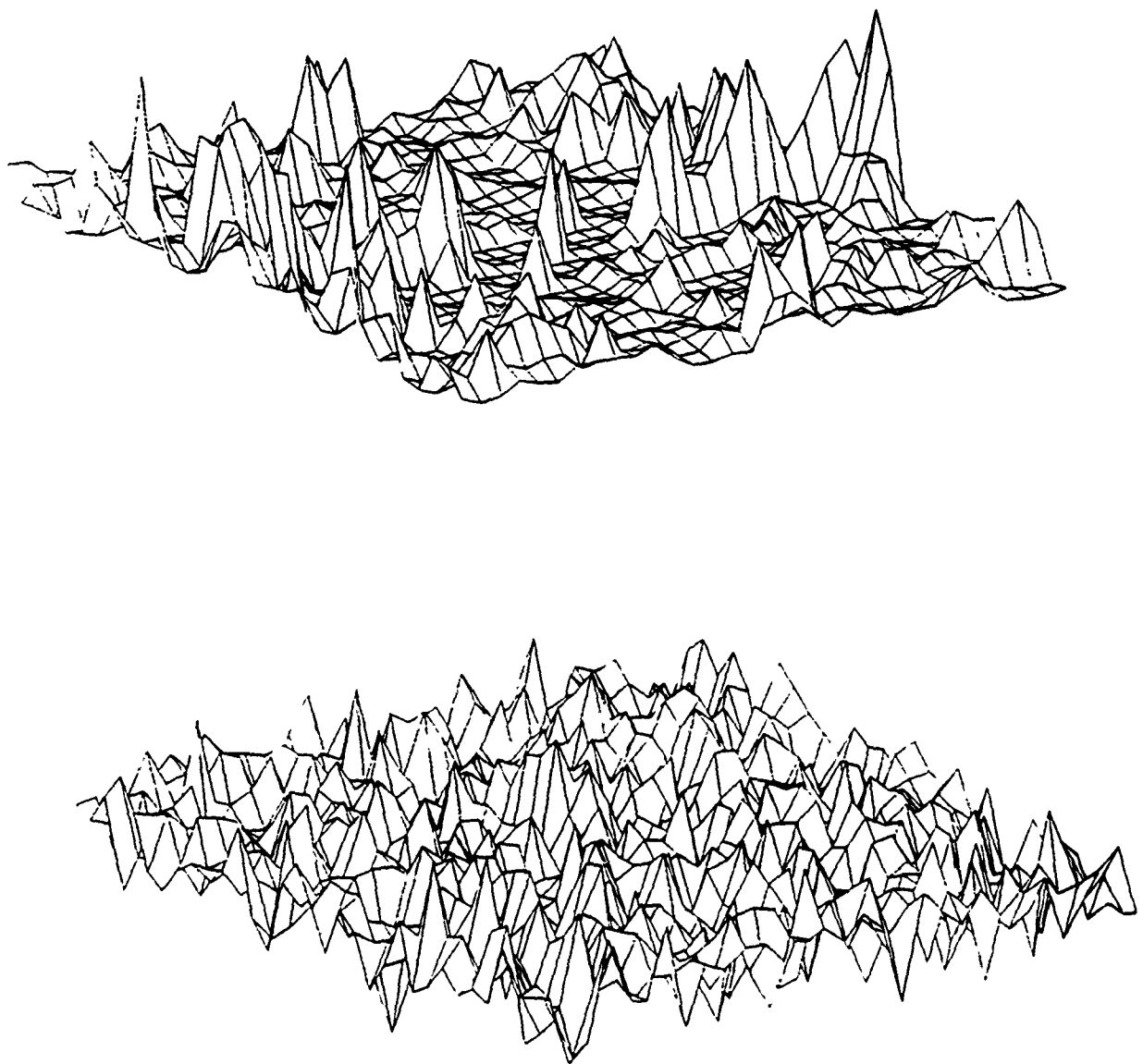


Figure 11: Estimated a) magnitude and b) phase spectrum

The phase of  $H(u, v)$  is

$$\begin{aligned} \theta_H(u + \delta u, v + \delta v) &= \theta_H(u, v) \\ &- [\theta_{G_i}(u, v) - \theta_{G_i}(u + \delta u, v + \delta v)]_{avg} \\ &+ [\theta_{F_i}(u, v) - \theta_{F_i}(u + \delta u, v + \delta v)]_{avg} \end{aligned}$$

Fig.11 shows the estimated  $32 \times 32$  magnitude and phase spectrum of  $H(u,v)$ .

### 5.4.2 Image Restoration

After identifying the magnitude and phase spectrum of  $H(u,v)$ , we can apply 32 x 32 dimension Wiener filter  $W_{32 \times 32}(u,v)$

$$W_{32 \times 32}(u,v) = \frac{H^*(u,v)}{|H(u,v)|^2 + \frac{S_{f_{32 \times 32}}(u,v)}{S_{n_{32 \times 32}}(u,v)}} \quad (35)$$

where  $S_{f_{32 \times 32}}(u,v)$  denote power spectral densities of the undegraded image and  $S_{n_{32 \times 32}}(u,v)$  denote power spectral densities of noise by selecting local smoothed 32 x 32 pixels region. Estimating power spectral densities by using Fast Fourier Transform is well documented in [9]. In our experiments, these power spectral densities are estimated by the following Periogram method.

$$S_{f_{32 \times 32}} = \frac{1}{N} \sum_{i=1}^N \frac{|F_i(u,v)|^2}{32 \times 32} \quad (36)$$

where  $N$  is the total number of subimages and  $F_i(u,v)$  is Fourier transformed  $i$ th subimage. After selecting smoothed 32 x 32 pixels region in the blurred image,  $S_{n_{32 \times 32}}(u,v)$  can be estimated by

$$S_{n_{32 \times 32}} = \frac{|N(u,v)|^2}{32 \times 32} \quad (37)$$

where  $N(u,v)$  is Fourier transformed noise region.

The estimated image  $F_e(u,v)$  is given by

$$F_e(u,v) = W_{32 \times 32}(u,v)G(u,v) \quad (38)$$

where  $G(u,v)$  is Fourier transformed blurred image. But the dimension of  $W_{32 \times 32}(u,v)$  is 32 x 32 and that of  $G(u,v)$  is 128 x 128. Hence we need to interpolate (or zoom)  $W_{32 \times 32}(u,v)$  into

$128 \times 128$  pixels dimension. Several image interpolation techniques are discussed in [6]. In our experiments, *bilinear* interpolation technique is used. This algorithm uses the four input pixels surrounding the point  $(i, j)$  to estimate the output pixel. After interpolate  $W_{32 \times 32}(u, v)$ , one can take Inverse Fourier transform to get restored image. The restored and contrast stretched images are shown in *Fig.12* and *Fig.13*.



(a)



(b)

Figure 12: Restored Image(Pseudocolored) by nonoverlapping subimage at (a) First (b) 32th Frame.

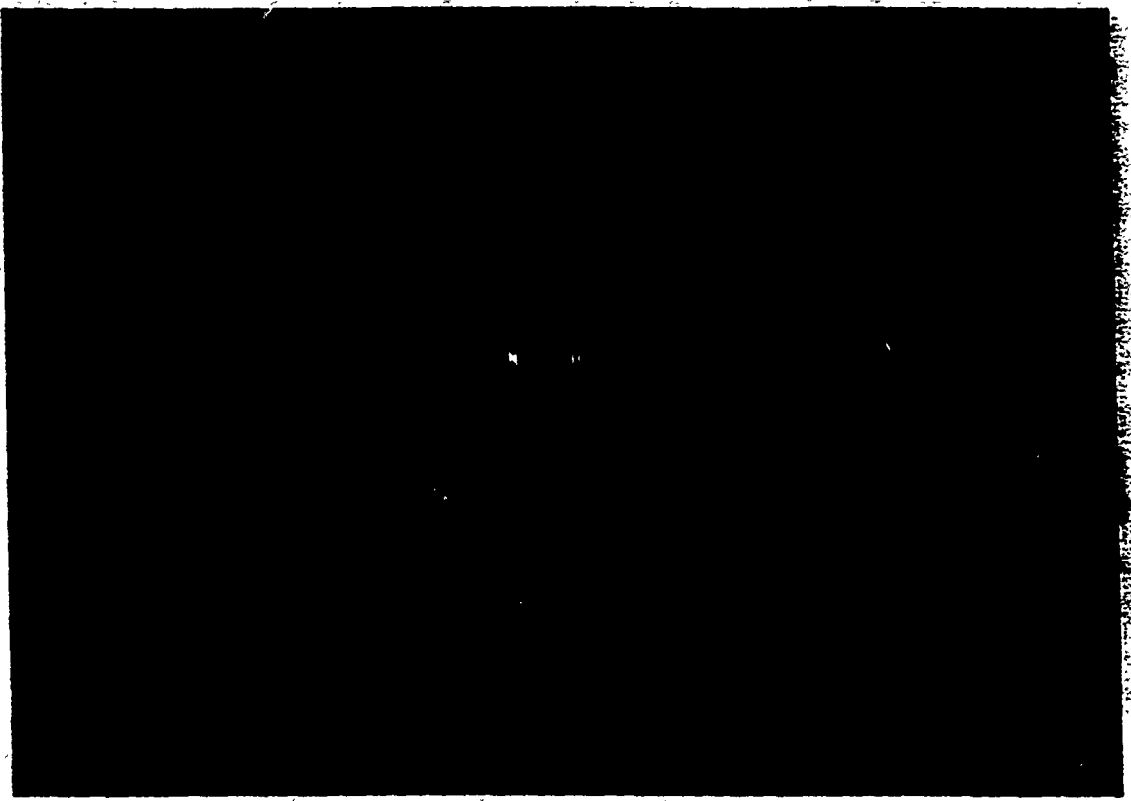
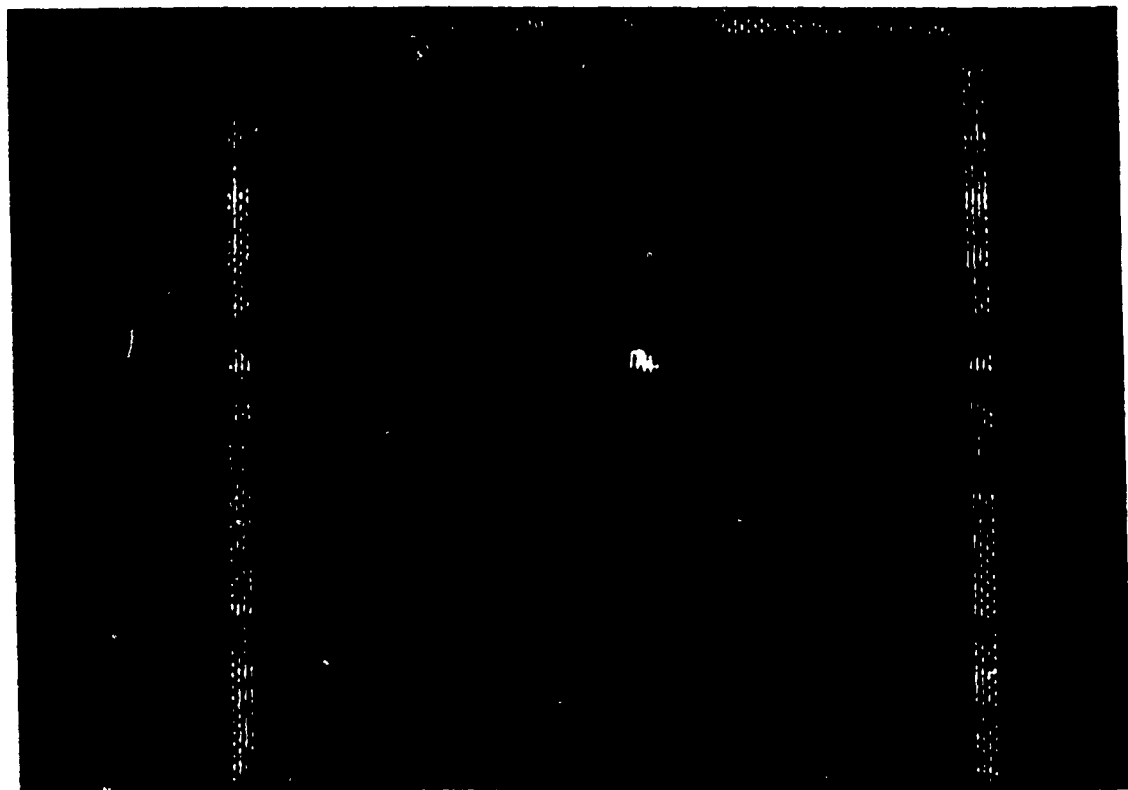


Figure 12 (c) Restored Image (Pseudocolored) by nonoverlapping at 69th Frame.



(a)



(b)

Figure 13: Restored Image (Pseudocolored) by 50 Percent overlapping at (a) First (b) 32th Frame.

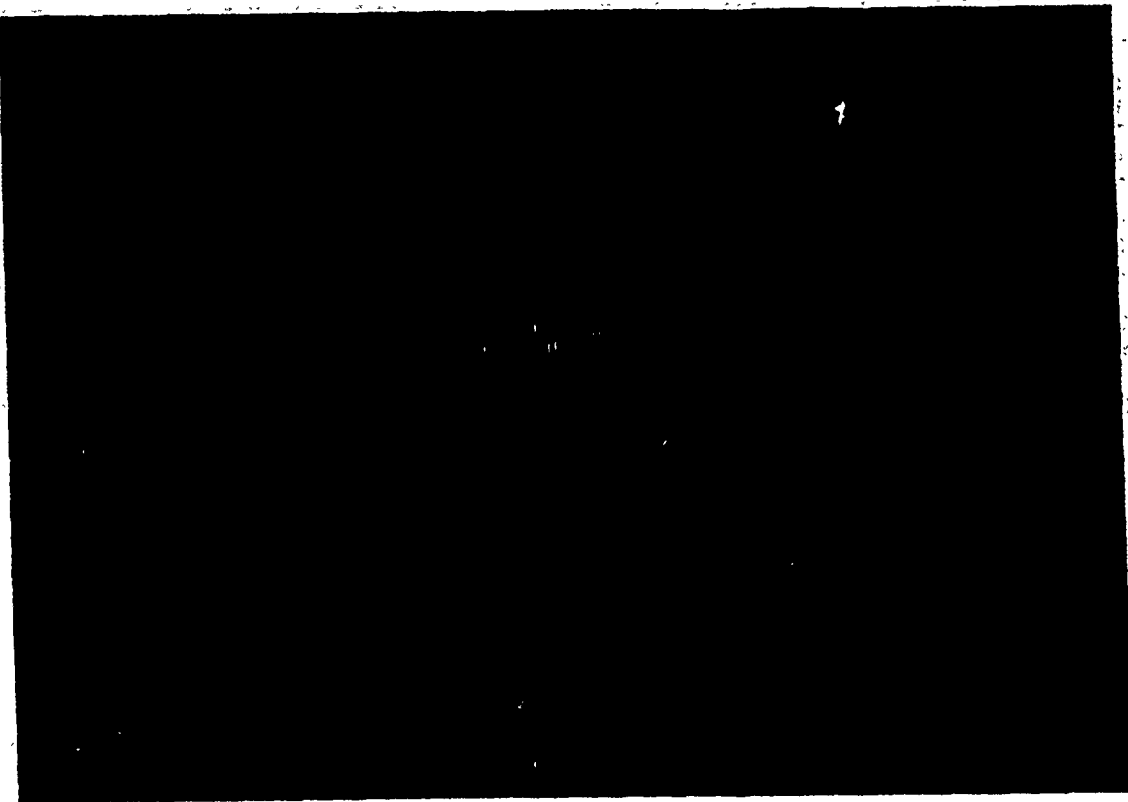


Figure 13. (c): Restored Image (Pseudocolored) by 50 Percent overlapping subimage at 69th Frame.

## 5.5 Conclusion

In this report, we can identify the mixing/shear layer blurring process *nonparametrically* by estimating the magnitude and phase spectrum of  $H(u, v)$ . By applying Wiener filter using global image statistics, we have restored image from the severely degraded image (See *Fig.6*).

In this restored image, the original target is clearly visible on the center. But it has a false slit pattern along the vertical axis and has one  $CO_2$  gas pattern. This false slit pattern might be come from utilizing global image statistics when one estimate Wiener filter. In the restored image as shown in *Fig.12* and *Fig.13*, several distinct  $CO_2$  gas patterns or objects are visible and bright spots related with original target are discerned around the center.

## References

- [1] J. Morton and H. Andrew. "*A posteriori method of image restoration*", *J. Opt. Soc. Am.*, vol. 69, no.2, Feb. 1979, pp280-290
- [2] T. Stockham and T. Cannon. "*Blind deconvolution through digital signal processing*," *Proc. IEEE*. vol. 63, pp. 678-692, April 1975
- [3] D. Ghiglia. "*Space invariant deblurring given N independently blurred images of a common object*". *J. Opt. Soc. Am.. A/vol.1. no.4. April 1984* pp 398-402
- [4] R. Gonzales. *Digital Image Restoration*. MA:Addison-Wesley, 1987
- [5] A. Jain. *Advances in mathematical models for image processing*," *Proc. IEEE*. vol. 69, pp 502-528. May 1981
- [6] A. Jain. *Fundamentals of Digital Image Processing* :Prentice Hall
- [7] J. Biemond, R. Lagendijk and R. Mersereau *Iterative methods for image deblurring*". *proc. IEEE*. vol. 78, no. 5. May 1990. pp 856-882
- [8] M. Sezan and A. Tekalp "Survey of recent developements in digital image restoration", *Optical Eng.*, vol. 29, no.5. May 1990
- [9] P. Welch "The use of Fast Fourier Transform for the Estimation of Power Spectra." *IEEE Trans.. ASSP 15*, pp 70-73 (1967)

**MUTUAL COHERENCE PROPAGATION IN  
TURBULENT MEDIA**

By

Anand C. Monteiro  
Department of Electrical and Computer Engineering  
University of Alabama in Huntsville  
Huntsville, AL 35899

John M. Jarem  
Department of Electrical and Computer Engineering  
University of Alabama in Huntsville  
Huntsville, AL 35899

## CONTENTS

- a) Task Objective: The overall purpose of the research is to create an algorithm which can generate optical or infrared images from a given source when the image passes through a thin layer which is highly turbulent. The turbulent layer is assumed to be induced by coolant passing over a hypervelocity optical window. The algorithm should be capable of studying image effects when the turbulence is inhomogeneous and anisotropic. The algorithm should also be capable of studying image effects as arise when the image passes through a bow shock region which precedes the turbulence layer and also study image effects as they occur when the image passes through a heated aero-optical window which occurs after the image has passed through the turbulence. The algorithm will be very useful for gauging how badly different hypervelocity aero-optical scenarios will effect image quality of different optical sensors.
  
- b) Technical Problems: The level of effort is mainly involved with theoretical optical analysis and numerical analysis. The main technical problems have concerned lack of adequate computer software on the UAH ECE ARDENT computer to perform analysis.
  
- c) General Methodology: The general methodology has been a theoretical and numerical optical analysis of image propagation in an inhomogeneous turbulence layer. The details of the analysis are given in the report.
  
- d) Technical Results: See attached report.
  
- e) Important Findings: See the conclusion of the attached report.

## ABSTRACT

The propagation of the Mutual Coherence Function is governed by a Partial Differential Equation. This equation can be solved by standard Finite Difference Techniques. For the case of propagation through homogeneous turbulence, it is also possible to obtain a closed form integrated solution. We show that it is necessary to split the Mutual Coherence Function into a delta and non-delta component. We obtain a differential equation for the non-delta component and compare the results obtained by an iterative solution and integrated solution.

## NOTATION

$j$	$= \sqrt{-1}$
$E(Z, X_1)$	= electric field at a point $(Z, X_1)$
$\Gamma_s(Z, X_1, X_2)$	$= \langle E(Z, X_1) E^*(Z, X_2) \rangle$ = ensemble average if the product of the electric fields at $E(Z, X_1)$ and $E(Z, X_2)$
$\Gamma_s(Z, X_c, X_d)$	= Spatial Domain mutual coherence function at $(Z, X_c, X_d)$
$X_c$	$= \frac{X_1 + X_2}{2}$
$X_d$	$= \frac{X_1 - X_2}{2}$
$\Gamma_f(Z, X_c, \kappa_c)$	= Fourier Domain MCF $= \frac{1}{2\pi} \int_{-\infty}^{\infty} \Gamma_s(Z, X_c, X_d) \exp(-j\kappa_c X_d) dX_d$
$\lambda$	= wavelength of radiation ( $m^{-1}$ )
$k$	$= 2\pi/\lambda$
$\ell_o$	= inner scale of turbulence ( $m^{-1}$ )
$L_o$	= outer scale of turbulence ( $m^{-1}$ )
$C_n^2$	= structure constant
$\zeta_m^2$	$= 5.92/\ell_o^2$
$\phi_n(\kappa)$	= spatial spectrum of the turbulence
$a(X_d)$	$= \int_{-\infty}^{\infty} \phi_n(\kappa) \exp(-j\kappa X_d) d\kappa$

## REPORT - ENDING SEPTEMBER 1990

### 1. INTRODUCTION

The image of an object, suffers an inevitable degradation, when it propagates through a turbulent medium. Such a medium is characterized by a randomly varying index of refraction. In the spectral domain, this varying index of refraction may be modeled by the Von Karman spectrum,  $\phi_n(\kappa)$ .

The Mutual Coherence Function (MCF), is an important tool with which to analyze the distortion suffered during the process of image formation. The propagation of the MCF is governed by a first order hyperbolic partial differential equation, which is applicable universally to the study of free space propagation and propagation through turbulence. The differential equation describes how the MCF is dependent on the spectrum of the refractive index.

In this report we are interested in studying the problem of what happens to an image when it passes through a thin layer of material which is highly turbulent. For present application the thin layer of material is formed by coolant passing over an aero-optical window. In our formulation, a coherent point source is situated at a distance  $L_s$  from a layer of turbulence of width  $L$ . We analyze the image formed at the plane  $L_s + L$ , by first computing the MCF in this plane. Once the image for a point source has been obtained, the image for any general object intensity distribution can be obtained by superposition from the point source solution.

At the present time, a closed form integrated solution is already available to compute the MCF for simple geometries like this. In this report we develop an alternative iterative solution for the MCF PDE, and compare the integrated and iterative solutions.

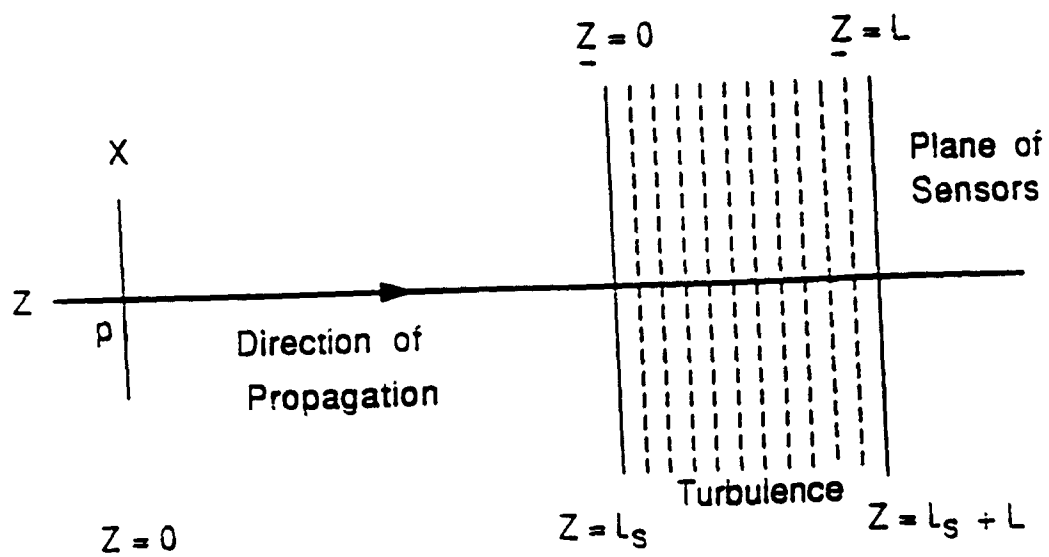


Fig. 1 Propagation through Homogeneous Turbulence.

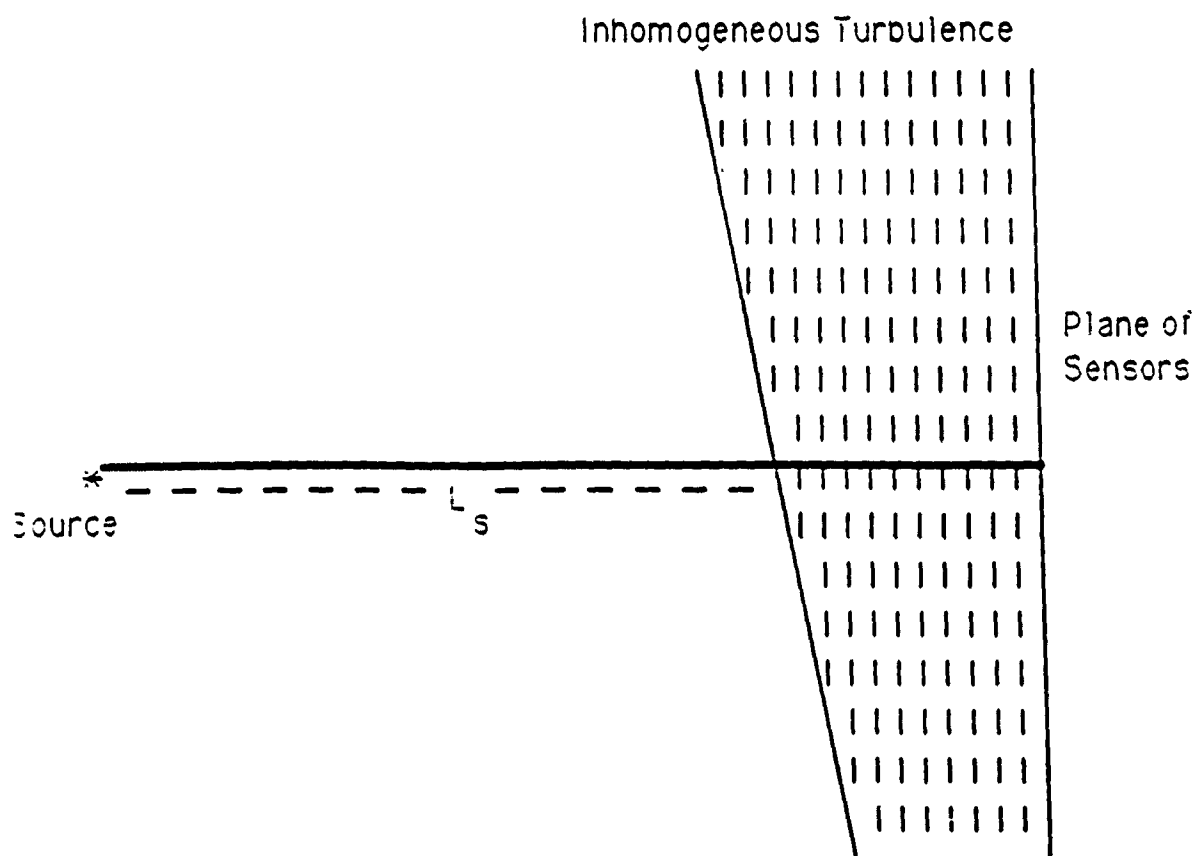


Fig. 2 Propagation through Inhomogeneous Turbulence.

The motivation for developing an iterative solution is so that in future analysis, layers of turbulence which are transversely inhomogeneous can also be studied with the aid of the iterative MCF formulation. The presently available integrated solution cannot be used for this purpose.

We show that the MCF can be expressed as the sum of a delta component and a non-delta component. This decomposition is shown to be an essential step for the practical numerical implementation of the iterative and the integrated solution methods. For a coherent point source, only the delta component is present for free space propagation. As the wave travels through turbulence, the non-delta component gradually gains strength, while the delta component wanes.

Further, it is shown in the report that the delta component represents the true image (without turbulence) of the point source, while the non-delta component contributes to the blur. Thus, as the wave propagates through the layer, the strength of the image point decreases, while the blur increases, due to the gain in strength of the non-delta component. Suggestions of how to apply the present theory to transversely inhomogeneous layers is given.

## 2. MATHEMATICAL PRELIMINARIES

### A. The Differential Equation for the Propagation of the MCF:

As shown in Fig. 1, a point source of light is situated at a distance  $L_s$  from a layer of turbulence. The direction of propagation of the light is orthogonal to the turbulent layer. Sensors are located at a point  $Z = L$  in the turbulent layer. We wish to find the MCF in the plane of the sensors. The turbulence is governed by the Von Karman spectrum,  $\phi_n(\kappa)$  [1, 2]. The MCF in the spatial domain  $\Gamma_s$ , is governed by the following partial differential equation [1, 2].

$$\left\{ 2jk \frac{\partial}{\partial Z} + \left[ \frac{\partial^2}{\partial X_1^2} - \frac{\partial^2}{\partial X_2^2} \right] - j\frac{k^3}{2} [a(0) - a(X_1 - X_2)] \right\} \Gamma_s(Z, X_1, X_2) = 0 \quad (1)$$

Where,  $\Gamma_s(Z, X_1, X_2) = \langle E(Z, X_1) E^*(Z, X_2) \rangle$  and other variables are defined in the Notation table. Now transforming to the  $(X_c, X_d)$  coordinate system, where,  $X_c = \frac{X_1 + X_2}{2}$  and  $X_d = \frac{X_1 - X_2}{2}$  we find

$$\left\{ 2jk \frac{\partial}{\partial Z} + 2 \frac{\partial^2}{\partial X_c \partial X_d} + j\frac{k^3}{2} [a(0) - a(X_d)] \right\} \Gamma_s(Z, X_c, X_d) = 0. \quad (2)$$

To proceed further we will express Eq. (2) in the spectral domain through the use of the following spatial Fourier transform:

$$\Gamma_s(Z, X_c, X_d) = \int_{-\infty}^{\infty} \Gamma_f(Z, X_c, \kappa_c) \exp[-jk_c X_d] d\kappa_c \quad (3)$$

and

$$a(X_d) = \int_{-\infty}^{\infty} \phi_n(\kappa) \exp(-jk_c X_d) d\kappa \quad (4a)$$

$$\phi_n(\kappa) = 0.033 C_n^2 (\kappa^2 + \frac{1}{L_o^2})^{-11/6} e^{-\kappa^2/\kappa_m^2} \quad (4b)$$

$$\kappa_m^2 = \frac{5.92}{L_o^2}.$$

After substituting (3) in (2), we apply the well known result, that the product of spatial domain terms,  $\Gamma_s(Z, X_c, X_d)$  and  $a(X_d)$  is equivalent to the convolution of the frequency domain terms,  $\Gamma_f(Z, X_c, \kappa_c)$  and  $\phi_n(\kappa)$  and obtain:

$$-2jk \frac{\partial \Gamma_f}{\partial Z} - 2j\kappa_c \frac{\partial \Gamma_f}{\partial X_c} - j\frac{k^3}{2} \left\{ a(0) \Gamma_f - \int_{-\infty}^{\infty} \Gamma_f(Z, X_c, \kappa'_c) \phi_n(\kappa_c - \kappa'_c) d\kappa'_c \right\} = 0 \quad (5a)$$

This equation describes the propagation of the MCF through homogeneous turbulence.

Since the focus of the report is on the study of propagation through inhomogeneous turbulence as well as homogeneous turbulence, we will now modify Eq. (5a) to account for the more general inhomogeneous case. Fig. 2 shows a more general case, where the turbulence layer is wedge shaped. To solve (5a), for turbulence of inhomogeneous geometry, we multiply the last term of Eq. (5a) with a function  $f(Z, X_c)$ :

$$-2jk \frac{\partial \Gamma_f}{\partial Z} - 2j\kappa_c \frac{\partial \Gamma_f}{\partial X_c} - j\frac{k^3}{2} f(Z, X_c) \left\{ a(0) \Gamma_f - \int_{-\infty}^{\infty} \Gamma_f(Z, X_c, \kappa'_c) \phi_n(\kappa_c - \kappa'_c) d\kappa'_c \right\} = 0 \quad (5b)$$

We have used the Von Karman spectrum to describe  $\phi_n(\kappa)$  and we model  $f(Z, X_c)$  by a polynomial function, which takes a value zero in free space and gradually attains a value of 1, as it enters deeper into the turbulence.

### B. The Integrated Solution for the Homogeneous Case [1] [2]:

An integrated solution  $\Gamma_f(Z, X_c, \kappa_c)$  of the (5), with  $f(Z, X_c) = 1$  (homogeneous case) has been shown to be [1, 2]:

$$\Gamma_f(Z, X_c, \kappa_c) = \frac{1}{2\pi k} \int_{-\infty}^{\infty} \exp[j\kappa_d(\frac{\kappa_c}{k}Z - X_c)] \exp[-H(\kappa_d, Z)] d\kappa_d \quad (6)$$

$$H(\kappa_d, Z) = \frac{k^2}{Z} \int_0^{\infty} \phi_n(\kappa) \left[ (Z - L_s) - \frac{\sin \left[ \frac{\kappa}{k} \kappa_d Z \right]}{\frac{\kappa}{k} \kappa_d} - \frac{\sin \left[ \frac{\kappa}{k} \kappa_d L_s \right]}{\frac{\kappa}{k} \kappa_d} \right] d\kappa \quad (7)$$

Although mathematically correct, computationally, (6) is not easy to handle, because it contains a delta component, and hence the integral in (6) does not converge in the ordinary sense. To see this, we note that in general

$$\lim_{\kappa_d \rightarrow \infty} H(\kappa_d, Z) = \frac{k^2}{2} (Z - L_s) \int_0^\infty \phi_n(\kappa) d\kappa \neq 0$$

Therefore, we must find a way to separate the delta and non-delta components in  $\Gamma_f(Z, X_c, \kappa_c)$ . Eqs. (6) and (7) may also be written in the form:

$$\begin{aligned} \Gamma_f(Z, X_c, \kappa_c) &= \frac{1}{2\pi k} \left\{ \int_{-\infty}^{\infty} \exp[j\kappa_d \left( \frac{\kappa_c}{k} Z - X_c \right)] \exp[-\frac{k^2}{4} a(0)(Z - L_s)] \right. \\ &\quad \left. \left[ \exp \left[ \frac{k^2}{4} \int_{L_s}^Z a \left( \frac{\kappa_d}{k} Z' \right) dZ' \right] - 1 \right] \right\} d\kappa_d \\ &+ \frac{1}{2\pi k} \left\{ \int_{-\infty}^{\infty} \exp[j\kappa_d \left( \frac{\kappa_c}{k} Z - X_c \right)] \exp[-\frac{k^2}{4} a(0)(Z - L_s)] \right\} d\kappa_d \end{aligned} \quad (8)$$

The second term in Eq. (8) is a well known representation of a delta function. Using this information we may write  $\Gamma_f$  as a sum of a non-delta component  $\Gamma'_f$  and a delta component  $T$ .

$$\Gamma_f(Z, X_c, \kappa_c) = \Gamma'_f(Z, X_c, \kappa_c) + T(Z, X_c, \kappa_c) \quad (9)$$

where

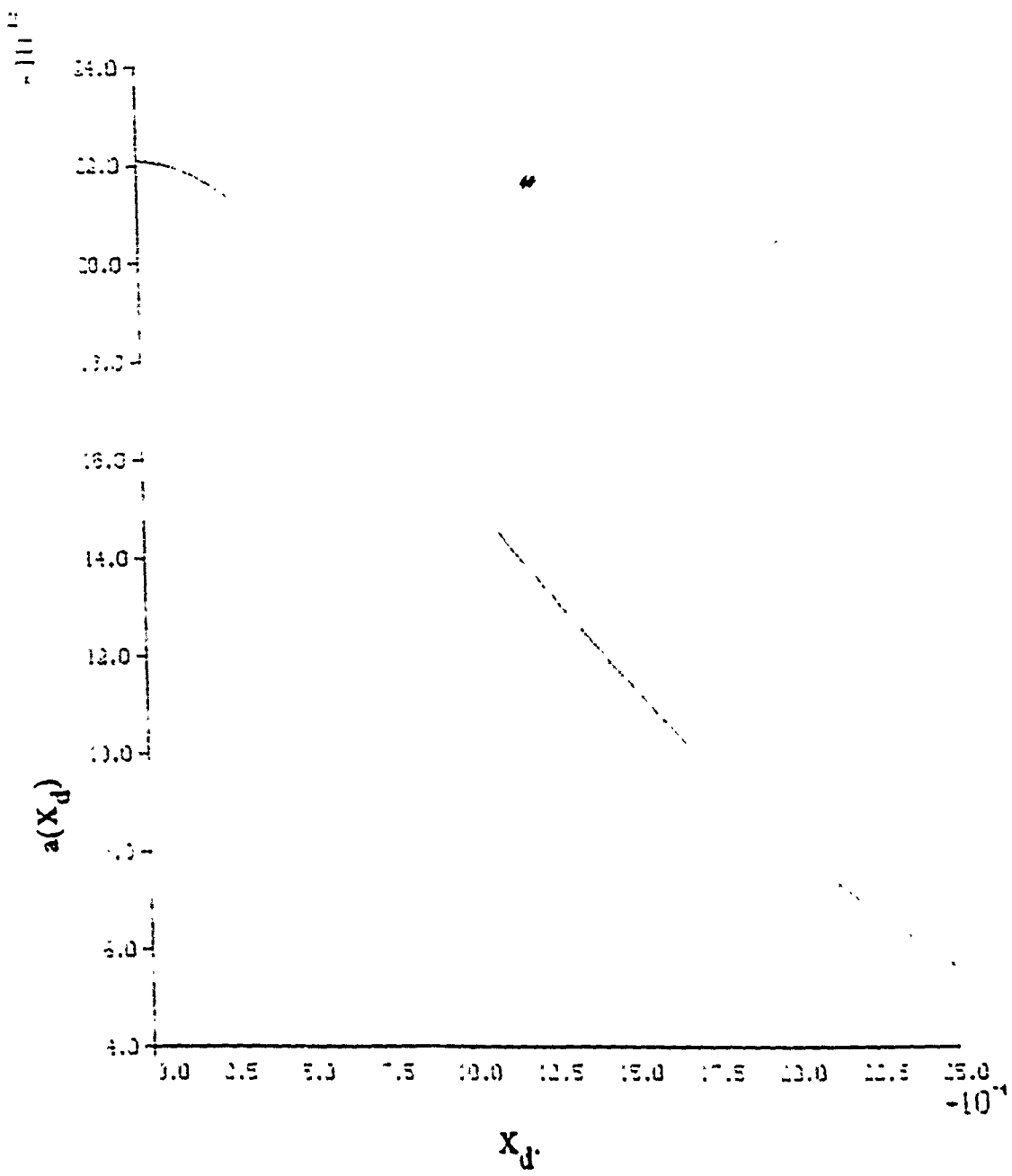


Fig. 3 Plot of  $a(X_d)$  versus  $X_d$ .

$$\Gamma'_f(Z, X_c, \kappa_c) = \frac{1}{2\pi k} \left\{ \int_{-\infty}^{\infty} \exp[j\kappa_d \left( \frac{\kappa_c}{k} Z - X_c \right)] \exp[-\frac{k^2}{4} a(0)(Z - L_s)] \right. \\ \left. \left[ \exp \left[ \frac{k^2}{4} \int_{L_s}^Z a \left( \frac{\kappa_d}{k} Z' \right) dZ' \right] - 1 \right] \right\} d\kappa_d \quad (10)$$

$$T(Z, X_c, \kappa_c) = \frac{1}{k} \exp[-\frac{k^2}{4} a(0)(Z - L_s)] \delta \left[ \frac{\kappa_c}{k} Z - X_c \right] \quad (11)$$

As opposed to Eq. (5), the Fourier Transform in Eq. (10) does converge. Consider the last term of the product.

$$\lim_{\kappa_d \rightarrow \infty} \left[ \exp \left[ \frac{k^2}{4} \int_{L_s}^Z a \left( \frac{\kappa_d}{k} Z' \right) dZ' \right] - 1 \right] = \exp(0) - 1 = 0$$

Since  $a(X)$  approaches zero as  $X$  approaches infinity (See Fig. 3), the integral in Eq. (10) does converge.

A further property of the integrated solution is that we need to carry out the integral in Eq. (10) only for  $X_c = 0$ . This results because of the form of  $\kappa_c$  and  $X_c$  in the argument of the first exponential of Eq. (10). If  $\Gamma'_{f0}$  is solution for  $\Gamma'_f$  at  $X_c = 0$ , then  $\Gamma'_f$  when  $X_c \neq 0$  is given by

$$\Gamma'_{f0}(Z, \kappa_c) = \Gamma'_f(Z, 0, \kappa_c) \\ \Gamma'_f(Z, X_c, \kappa_c) = \Gamma'_{f0}(Z, \kappa_c - \frac{k}{Z} X_c). \quad (12)$$

Next we develop an iterative solution for  $\Gamma'_f$ . It is one of the goals of our work to compare the iterative solution, with the integrated solution, given by (10).

### C. The Iterative Solution

To find the iterative solution for the homogeneous case, we set  $f(Z, X_c) = 1$  and apply the PDE given by (5), to each of the components of  $\Gamma_f(Z, X_c, \kappa_c)$ . Substituting  $\Gamma_f = \Gamma'_f + T$  into Eq. 5a we have:

$$\begin{aligned} & \frac{\partial}{\partial Z} (\Gamma'_f + T) + \frac{\kappa_c}{k} \frac{\partial}{\partial X_c} (\Gamma'_f + T) \\ & + \frac{k^2}{4} \left\{ a(0)(\Gamma'_f + T) - \int_{-\infty}^{\infty} [\Gamma'_f(Z, X_c, \kappa'_c) + T(Z, X_c, \kappa'_c)] \phi_n(\kappa_c - \kappa'_c) d\kappa'_c \right\} = 0 \end{aligned} \quad (13)$$

Rearranging terms.

$$\begin{aligned} & \left\{ \frac{\partial T}{\partial Z} + \frac{\kappa_c}{k} \frac{\partial T}{\partial X_c} + \frac{k^2}{4} \left[ a(0) T - \int_{-\infty}^{\infty} T(Z, X_c, \kappa'_c) \phi_n(\kappa_c - \kappa'_c) d\kappa'_c \right] \right\} \\ & + \left\{ \frac{\partial \Gamma'_f}{\partial Z} + \frac{\kappa_c}{k} \frac{\partial \Gamma'_f}{\partial X_c} + \frac{k^2}{4} \left[ a(0) \Gamma'_f - \int_{-\infty}^{\infty} \Gamma'_f(Z, X_c, \kappa'_c) \phi_n(\kappa_c - \kappa'_c) d\kappa'_c \right] \right\} = 0 \end{aligned} \quad (14)$$

Denoting the terms in the first set of braces by  $Q(Z, X_c, \kappa_c)$  and rearranging (14):

$$\frac{\partial \Gamma'_f}{\partial Z} + \frac{\kappa_c}{k} \frac{\partial \Gamma'_f}{\partial X_c} + \frac{k^2}{4} \left\{ a(0) \Gamma'_f - \int_{-\infty}^{\infty} \Gamma'_f(Z, X_c, \kappa'_c) \phi_n(\kappa_c - \kappa'_c) d\kappa'_c \right\} = -Q(Z, X_c, \kappa_c) \quad (15)$$

and

$$Q(Z, X_c, \kappa_c) = \frac{\partial T}{\partial Z} + \frac{\kappa_c}{k} \frac{\partial T}{\partial X_c} + \frac{k^2}{4} \left[ a(0) T - \int_{-\infty}^{\infty} T(Z, X_c, \kappa'_c) \phi_n(\kappa_c - \kappa'_c) d\kappa'_c \right] \quad (16)$$

We use Eq. (11) for  $T$  and obtain  $\frac{\partial T}{\partial Z}$  and  $\frac{\partial T}{\partial X_c}$ :

$$\begin{aligned}\frac{\partial T}{\partial Z} = & -\frac{k^2}{4} a(0) \exp \left[ -\frac{k^2}{4} a(0)(Z - L_s) \right] \delta \left[ \frac{\kappa_c}{k} Z - X_c \right] \\ & + \frac{\kappa_c}{k^2} \exp \left[ -\frac{k^2}{4} a(0)(Z - L_s) \right] \delta' \left[ \frac{\kappa_c}{k} Z - X_c \right]\end{aligned}\quad (17)$$

$$\frac{\kappa_c}{k} \frac{\partial T}{\partial X_c} = -\frac{\kappa_c}{k^2} \exp \left[ -\frac{\kappa_c}{k^2} a(0)(Z - L_s) \right] \delta' \left[ \frac{\kappa_c}{k} Z - X_c \right] \quad (18)$$

Using (17) and (18) in (16), we find that the delta functions drop out and that  $Q$  is given by

$$Q = -\frac{k^2}{4} \int_{-\infty}^{\infty} T(Z, X_c, \kappa'_c) \phi_n(\kappa_c - \kappa'_c) \quad (19)$$

Again using the expression for  $T$  in (11) and integrating (19) we find

$$Q(Z, X_c, \kappa_c) = -\frac{k^2}{4} \exp \left\{ -\frac{k^2}{4} a(0)(Z - L_s) \right\} \phi_n(\kappa_c - \frac{k}{Z} X_c) \quad (20)$$

The nonhomogeneous right hand side of Eq. (15) which results from integration over the  $T$  delta function can be thought of as a source which excites  $\Gamma'_f$  as the wave propagates in the medium. Because  $T$  of Eq. (11) decreases with increasing  $Z$ , one can think of energy as being transferred from the  $T$  delta function (coherent energy) to the incoherent part of the wave  $\Gamma'_f$  (incoherent part of the wave). It is interesting that the spectrum of the turbulence itself determines how the incoherent energy  $\Gamma'_f$  is generated. Now substituting (20) into (15) gives

$$\begin{aligned}
& \frac{\partial \Gamma_f'}{\partial Z} + \frac{\kappa_c}{k} \frac{\partial \Gamma_f'}{\partial X_c} + \frac{k^2}{4} \left\{ a(0) \Gamma_f' - \int_{-\infty}^{\infty} \Gamma_f'(Z, X_c, \kappa_c') \phi_n(\kappa_c - \kappa_c') d\kappa_c' \right\} \\
& = \frac{k^2}{4Z} \exp \left\{ -\frac{k^2}{4} a(0)(Z - L_s) \right\} \phi_n(\kappa_c - \frac{k}{Z} X_c)
\end{aligned} \tag{21}$$

We now discretise this equation at the point  $(Z_{n+1}, X_{cm}, \kappa_{cl})$  and we define

$$\Delta Z = Z_{n+1} - Z_n \quad \Delta X_c = X_{cm+1} - X_{cm} \quad \Delta \kappa_c = \kappa_{cl+1} - \kappa_{cl} \tag{22}$$

The discretised system now becomes:

$$\begin{aligned}
& \Gamma_f'(Z_{n+1}, X_{cm}, \kappa_{cl}) \left\{ \frac{k^2}{4} a(0) + \frac{1}{\Delta Z} \right\} - \frac{k^2}{4} \sum_{q=-\infty}^{\infty} \Gamma_f'(Z_{n+1}, X_{cm}, \kappa_{cq}) \phi_n(\kappa_{cl} - \kappa_{cq}) \\
& = \frac{k^2}{4Z_{n+1}} \exp \left\{ -\frac{k^2}{4} a(0)(Z_{n+1} - L_s) \right\} \phi_n(\kappa_{cl} - \frac{k}{Z_{n+1}} X_{cm}) + \frac{1}{\Delta Z} \Gamma_f'(Z_n, X_{cm}, \kappa_{cl}) \\
& \quad - \frac{\kappa_{cl}}{2k \Delta X_c} \left\{ \Gamma_f'(Z_n, X_{cm+1}, \kappa_{cl}) - \Gamma_f'(Z_n, X_{cm-1}, \kappa_{cl}) \right\}
\end{aligned} \tag{23}$$

The initial condition is:

$$\Gamma_f'(L_s, X_c, \kappa_c) = 0 \tag{24}$$

The system (23) is a backward difference scheme for approximating PDE's. The convolution, when discretised leads to the well-known Toeplitz matrix, whose elements are various values of the function  $a(X_d)$ . This matrix remains the same throughout the computation and needs to be inverted only once.

### 3. EXAMPLES AND RESULTS

In this section, we present a few examples and results. We solve a homogeneous problem, typified by Fig. 2, and compare the results obtained from the iterative solution, which is set up in equation (23), with the results obtained from the integrated solution in Eq. (10).

For all the examples we use the following values for the parameters:

$$\begin{aligned} L_s &= 1000 \text{ m} \\ \lambda &= 5.5 \times 10^{-7} \text{ m (5500\text{\AA})} \\ C_n &= 0.2 \text{ m}^{-1/3} \\ \ell_o &= 10^{-5} \text{ m} \\ L_o &= 0.001 \text{ m} \\ \Delta X_c &= 10^{-3} \text{ m} \\ \Delta Z &= 10^{-4} \text{ m} \\ \Delta \kappa_c &= 50 \text{ m}^{-1} \end{aligned}$$

Fig. 4 shows how the strength of the delta function  $T(Z, 0, 0)$  drops as it propagates through the turbulent layer.  $Z$  is the distance in the turbulent layer and  $Z = L_s + \underline{Z}$ .

Fig. 5 is a plot of the non-delta component,  $\Gamma'_f(\underline{Z}, 0, 0)$  ( $Z = L_s + \underline{Z}$ ,  $X_c = 0$ ,  $\kappa_c = 0$ ). There are two completing processes:  $\Gamma'_f$  continually gains energy from the delta component  $T(Z, X_c, \kappa_c)$ , but also loses energy as it propagates through the turbulence. Since, we have seen in Fig. 4, that the strength of  $T(Z, X_c, \kappa_c)$  continually decreases, there comes a point where the loss of energy to the turbulence cannot be offset by a gain of energy from  $T(Z, X_c, \kappa_c)$  and  $\Gamma'_f$  starts to decrease.

Fig. 6 is a 3-D plot of  $\Gamma'_f(\underline{Z}, 0, \kappa_c)$  from  $\underline{Z} = 0$  to  $\underline{Z} = 3 \times 10^{-3}$  mm.

Fig. 7 is a 3-D plot of  $\Gamma'_f(\underline{Z}, 10, \kappa_c)$  and with  $\Delta X_c = 0.001$  metres, this shows how  $\Gamma'_f$  changes at off center point, meters away from the origin.

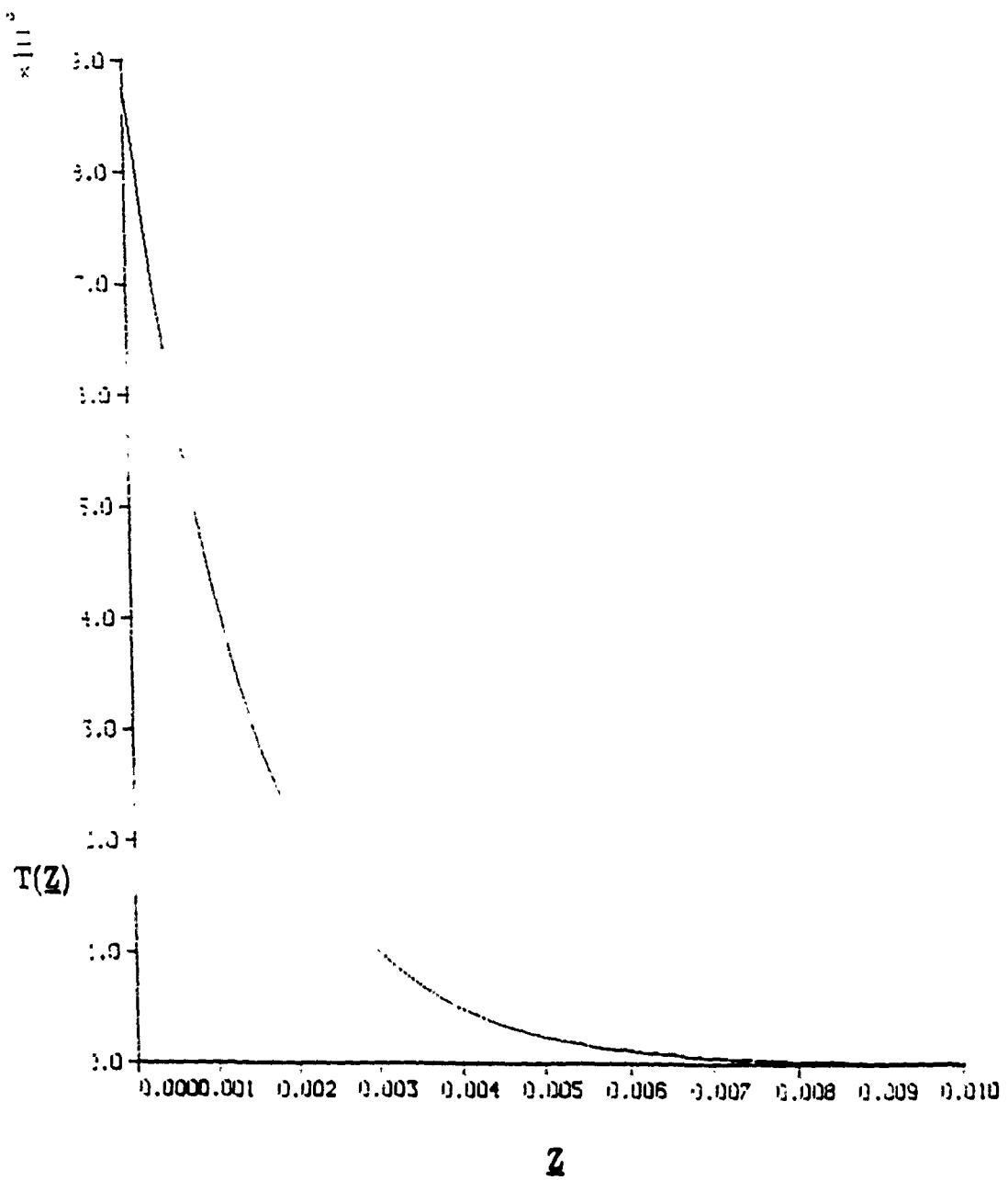


Fig. 4  $T(Z)$  at  $X_c = 0$ ,  $\kappa_c = 0$  versus  $Z$ , where  $Z$  = distance in the turbulent layer and  $Z = L_s + \underline{Z}$ .

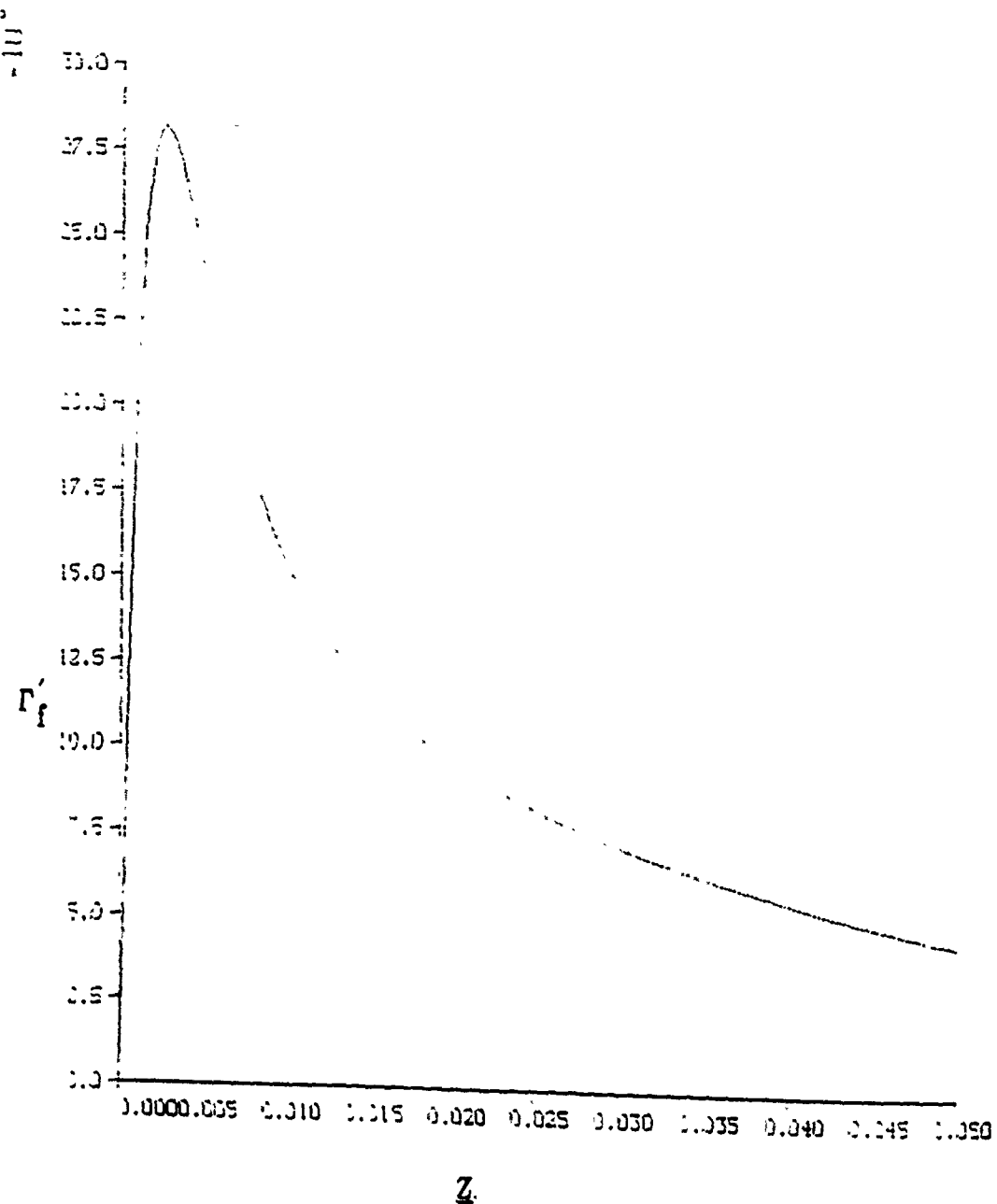


Fig. 5       $\Gamma_f'(Z)$  at  $X_c = 0$ ,  $\kappa_c = 0$  versus  $Z$ .  $Z = L_s + Z$ .

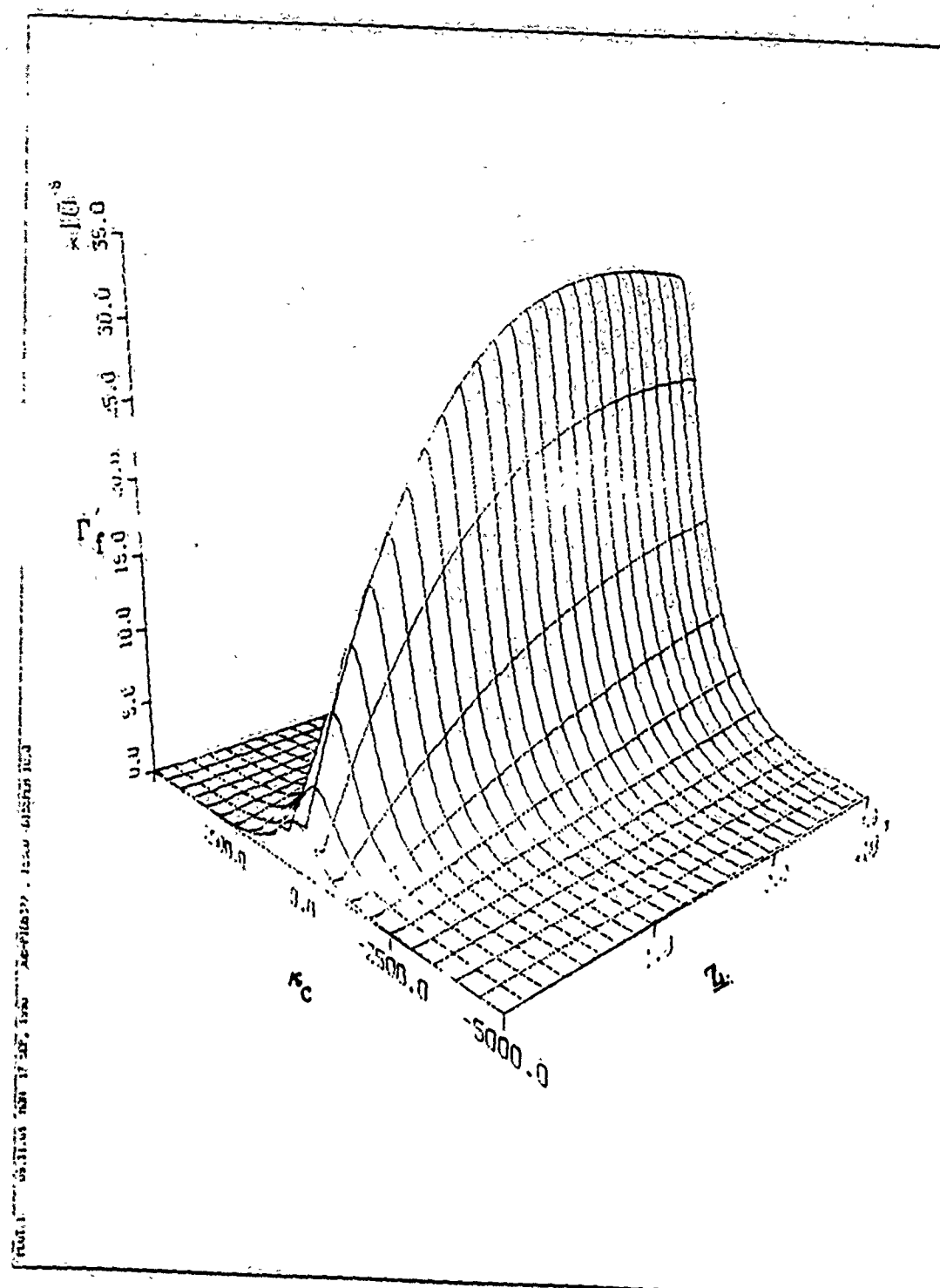


Fig. 6      A 3-D plot of  $\Gamma_f(Z, \kappa_c)$  at  $X_c = 0$  meters.

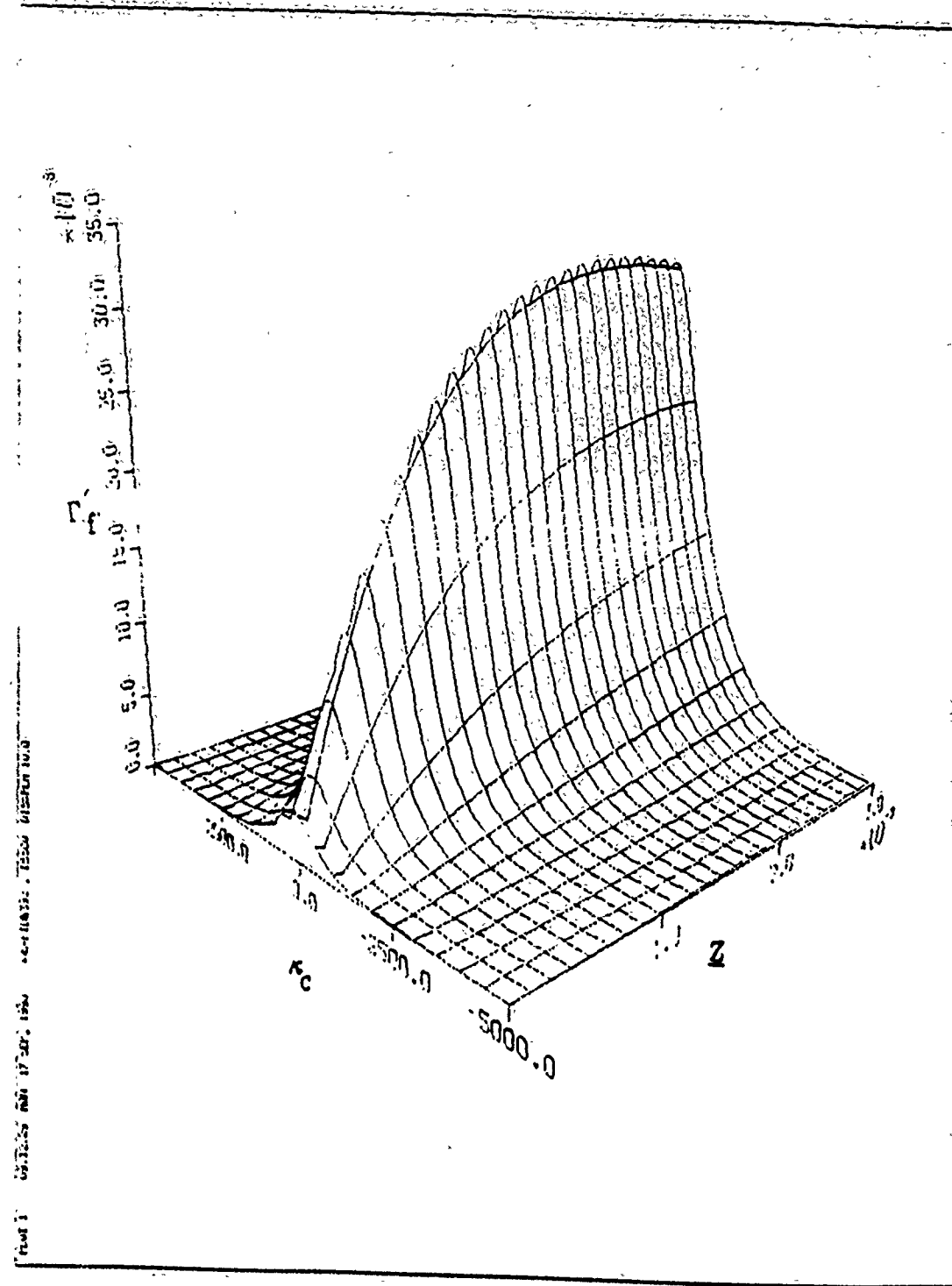


Fig. 7      A 3-D plot of  $\Gamma_f(Z, \kappa_c)$  at  $X_c = 0.01$  meters.

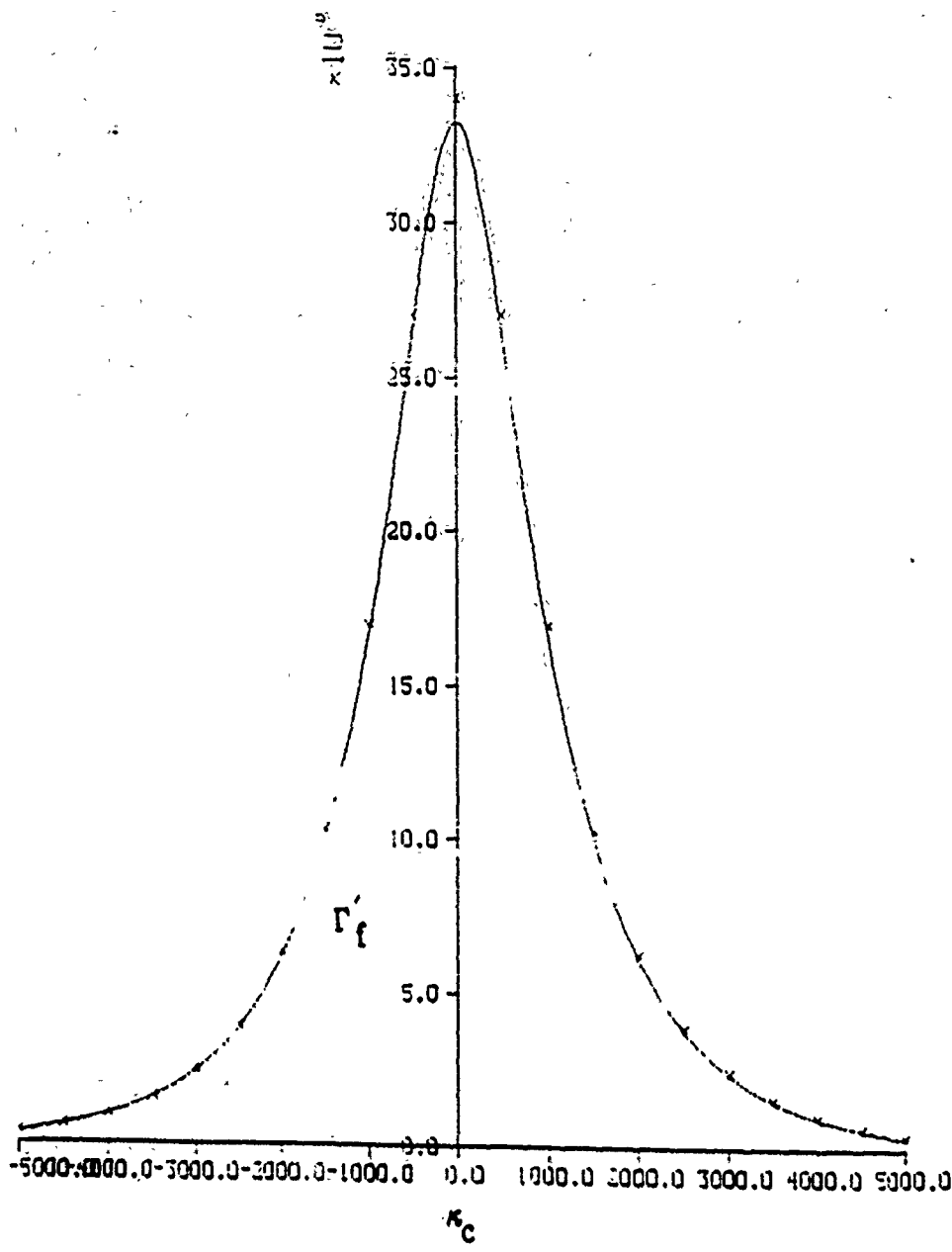


Fig. 8 Comparison of the integrated and iterative solutions at a distance  $Z = 3 \times 10^{-3}$  meters in the layer. The continuous curve is the iterative solution, while the asterisks represent the integrated solution.

Fig. 8 is a comparison of the iterative and integrated solution for  $Z = 3 \times 10^{-3}$  m,  $X_c = 0$ . The continuous curve is the iterative solution, while the asterisks represent the integrated solution.

#### 4. CONCLUSIONS

We have solved the differential equation governing the propagation of the Mutual Coherence Function in the frequency domain, by two techniques: an iterative method and a closed form integrated method. The results from both these methods agree extremely well.

It was necessary to split the MCF into two components: a delta component and a non-delta component. In free space, only the delta component is present and a point source images to a point, if diffraction at a lens aperture is ignored.

In a turbulent medium, the non-delta component  $\Gamma'_f$  is a significant factor. It grows in strength by absorbing energy from the delta component, until it reaches a maximum. Simultaneously, it also loses energy to the medium by scattering. After reaching a maximum  $\Gamma'_f$  gradually falls off.

The delta component will still image to a point, with greatly diminished strength, while the  $\Gamma'_f$  will contribute to fuzziness in the image.

#### 5. FUTURE WORK

We intend to study the propagation of the MCF, for inhomogeneous turbulence. We will then construct an image of a point source, after propagation of the wave through the inhomogeneous turbulence.

We have concentrated our efforts, so far on two dimensional models. The next step will be to analyze the more difficult three dimensional case.

## REFERENCES

- [1] Jarem, J. and Monteiro A., Chapter 5, Technical Report, 1989.
- [2] Ishimaru A., Wave Propagation and Scattering in Random Media, Vol. 2, Academic Press, New York, 1978.

Figure Captions

- Fig. 1 Propagation in Homogeneous Turbulence.
- Fig. 2 Propagation in Inhomogeneous Turbulence.
- Fig. 3 Plot of  $a(X_d)$  versus  $X_d$ .
- Fig. 4  $T(\underline{Z})$  at  $X_c = 0$ ,  $\kappa_c = 0$  versus  $\underline{Z}$ , where  $\underline{Z} =$  distance in the turbulent layer and  $Z = L_s + \underline{Z}$ .
- Fig. 5  $\Gamma_f'(\underline{Z})$  at  $X_c = 0$ ,  $\kappa_c = 0$  versus  $\underline{Z}$ .  $Z = L_s + \underline{Z}$ .
- Fig. 6 A 3-D plot of  $\Gamma_f'(\underline{Z}, \kappa_c)$  at  $X_c = 0$  meters.
- Fig. 7 A 3-D plot of  $\Gamma_f'(\underline{Z}, \kappa_c)$  at  $X_c = 0.01$  meters.
- Fig. 8 Comparison of the integrated and iterative solutions at a distance  $\underline{Z} = 3 \times 10^{-3}$  meters in the layer. The continuous curve is the iterative solution, while the asterisks represent the integrated solution.